An effective numerical strategy for retrieving all characteristic parameters of an elastic scatterer from its FFP measurements

Izar Azpiroz, Hélène Barucq, Julien Diaz, Rabia Djellouli

HAL Id: hal-02961043

https://hal.inria.fr/hal-02961043

Submitted on 8 Oct 2020

An Effective Numerical Strategy for Retrieving all Characteristic Parameters of an Elastic Scatterer from its FFP Measurements.

Izar Azpiroz[a], Hélène Barucq[b], Julien Diaz[b], Rabia Djellouli[*,c]

[a]*Vicomtech Foundation, Basque Research and Technology Alliance (BRTA), Mikeletegi 57, 20009 Donostia-San Sebastián, Spain*
[b]*Inria, E2S UPPA, Université de Pau et des Pays de l'Adour, Team Magique-3D, LMAP, Avenue de l'Université, BP 1155, 64013 PAU Cedex France*
[c]*Department of Mathematics and Interdisciplinary Research Institute for the Sciences, IRIS, California State University, 18111 Nordhoff Street, Northridge, CA 91330, USA*

Abstract

A new computational strategy is proposed for determining all elastic scatterer characteristics including the shape, the material properties (Lamé coefficients and density), and the location from the knowledge of far-field pattern (FFP) measurements. The proposed numerical approach is a multi-stage procedure in which a carefully designed regularized iterative method plays a central role. The adopted approach is critical for recognizing that the different nature and scales of the sought-after parameters as well as the frequency regime have different effects on the scattering observability. Identification results for two-dimensional elastic configurations highlight the performance of the designed solution methodology.

Keywords: Helmholtz equation, Elastic scatterer, Inverse scattering problem, Ill-posedness, Regularization, Pseudoinverses, Newton-type method

Introduction

Inverse scattering problems, where information about an unknown object such as a body, or an inhomogeneity in a material, or a potential, is to be recovered from measurements of waves of fields scattered by this object, are fundamental for exploring objects that are not accessible to *in situ* measurements. This class of problems is notoriously very difficult to investigate mathematically and/or numerically [1]. The challenge is due to the fact that these problems are not only nonlinear but also ill-posed in the sense of Hadamard [2]. In spite of their difficulties, inverse scattering problems received a great deal of attention by mathematicians, scientists, and engineers, as attested by the prolificness of papers and conferences dedicated to this topic. This is due in part to their relevance to a wide range of important applications including seismology [3, 4], radar and sonar [5], optics [6], along with many other areas in science and medical imaging technology.

The inverse scattering problem considered in this paper consists in retrieving *all* the properties of an elastic scatterer that lies in an acoustic medium from the knowledge of its full aperture far-field pattern

---

*Corresponding author
Email addresses: `iazpiroz@vicomtech.org` (Izar Azpiroz), `helene.barucq@inria.fr` (Hélène Barucq), `julien.diaz@inria.fr` (Julien Diaz), `rabia.djellouli@csun.edu` (Rabia Djellouli*,)

(FFP) measurements corresponding to one or multiple incident plane waves (see Section 2). Hence, the prototype mathematical problem is made of the Navier equation, to model propagation in an elastic medium, coupled with the Helmholtz equation that describes the propagation in a acoustic medium. Unlike the case of time-domain scattering problems [7], the full identification of an elastic obstacle has not been previously addressed in the case of time-harmonic scattering problems. This work constitutes the first numerical attempt to simultaneously recover all the object properties: the shape of the scatterer, its material properties (Lamé coefficients and the density), and its location characterized here by the origin of the coordinate system of the scatterer. All existing numerical methods have been designed and so far employed for only partial parameters reconstruction. More specifically, extensive efforts have been devoted during the past five decades to the determination of the shape of an unknown object from the knowledge of its corresponding FFP measurements and the nature of the object. Indeed, various computational procedures have been designed for this purpose (see, e.g., [8, 9, 10, 11, 12, 13, 14, 15, 16, 17, 18, 19], and the references therein). Note that in spite of the absence of a rigorous proof of their convergence [20], regularized Newton-type methods have been among the primary candidates for solving inverse obstacle problems (IOP) (see, e.g., [9, 21, 22, 23, 24, 25, 26, 27, 28]). This is due to the fact that the Newton aspect addresses effectively the nonlinearity of these IOPs whereas the regularization procedure restores the stability. Note that a new class of numerical methods has been very recently designed with the feature to be "globally convergent". The most advanced among these methods is the so-called convexification method presented in [29, 30] for the case of a single incident plane wave. For this method, it is proved that if a gradient projection method starts at an arbitrary point, this method converges to the time solution. So far, the case of Lamé coefficients has not been handled by the convexification method. The problem of finding the material parameters (Lamé coefficients and the density) of elastic scatterers has also been extensively studied and a wide range of numerical techniques have been developed to address it (see, e.g., [31, 32, 33, 34] and the references therein). Likewise, various numerical approaches have been proposed to locate objects from the knowledge of their corresponding FFP measurements and the nature of the objects, as reported in [35, 36, 37, 38, 39, 40, 41], among other references. To conclude, reference [42] is the only paper that we have encountered in the literature that proposes, for time-harmonic inverse problem, a technique to reconstruct simultaneously the shape of an object along with the two parameters that characterize the impedance boundary condition adopted in the considered mathematical model. Note that for time-domain problems, the identification method proposed in [43] has been designed to determine more than just the location of the scatterer. We have not come across of any work about fully identifying the inverse time-harmonic scattering problem considered in Section 2 and delivering the full characteristics of elastic scatterers from their FFP measurements.

Given that, our goal is to propose a solution methodology to fully recover the properties of an elastic object from the knowledge of its corresponding FFP measurements. The proposed approach is a multi-stage strategy in which a carefully designed regularized Newton-type algorithm plays a central role (see Section 3). The idea of using regularized Newton-type methods for solving inverse scattering problems is

not new. The novelty here is that it is employed in a multi-stage context in order to recognize that the sought-after parameters (shape parameters, material parameters, location parameters) have, depending on the frequency regime, different influences on the scattering observability. The proposed strategy delivers in its first stage the shape and material parameters and then the scatterer's location, defined here by the origin of the coordinate system for the obstacle, is obtained in the second stage. Note that the scale variability of the parameters is addressed here via a rescaling procedure applied to the forward problems (see Section 1.3), whereas an appropriate choice of the regularization matrix addresses the sensitivity to the sought-after parameters' influence on the reconstruction (see Section 3.3).

The remainder of the paper is organized as follows. In Section 1, we specify the nomenclature and assumptions adopted in this paper. We then state the forward scattering problem and introduce the rescaling procedure employed to address the scale variability of the scatterer's parameters. Last, we formulate the considered inverse scattering problem. Section 2 is devoted to the description of the designed solution methodology and its salient features. The main calculations required by the proposed inversion solver are described in Section 3. These are (a) the evaluation of the Jacobian matrix entries, (b) the solution of the forward problems that occur at each Newton iteration, and (c) the computation of the regularization matrix entries. A summary describing this new inversion algorithm along with its computational complexity are reported in Section 4. We present in Section 5 illustrative numerical parameters recovery for various scatterer's configurations including a non-convex octagon and a mock-up submarine. The considered scatterers are respectively made of steel and aluminum. These identifications have been performed using FFP measurements tainted with noise level ranging from 0% to 15%. The obtained results highlight the performance effectiveness of the proposed multi-stage solution methodology.

1. Preliminaries

We first introduce the notations and the assumptions we adopt throughout this paper. We then state the mathematical formulation of the elasto-acoustic time-harmonic scattering problem and its nondimensionalized version. Last, we formulate the considered inverse problem.

1.1. Nomenclature and Assumptions

Throughout this section, we adopt the following nomenclature and assumptions:

- Ω^s is a bounded domain of $\mathbb{R}^2$ representing an elastic obstacle.

- Ω^f is an infinite domain representing the fluid that surrounds Ω^s, i.e., $\Omega^f = \mathbb{R}^2 \setminus \overline{\Omega}^s$.

- Γ is the boundary of Ω^s and is assumed to be Lipschitz continuous.

- Σ is the exterior artificial boundary. Σ is a circle.

- $\boldsymbol{x} = (x_1, x_2)^T$ is a point of $\mathbb{R}^2$ and $r = \| \boldsymbol{x} \|_2$ is the distance from the origin point to $\boldsymbol{x}$ (m).

- S^1 is the unit circle in $\mathbb{R}^2$, i.e., $S^1 = \{\boldsymbol{x} \in \mathbb{R}^2,\ \|\ \boldsymbol{x}\ \|_2 = 1\}$.

- ∇ (resp. Δ) is the gradient (resp. Laplace) operator in $\mathbb{R}^2$.

- ν is the outward normal to the boundaries Γ and Σ, and $\dfrac{\partial}{\partial \nu}$ is the normal derivative operator.

- k is a positive number representing the wavenumber of the incident plane wave (m^{-1}) . $k = \dfrac{2\pi f}{c_f}$, where f is the frequency of the propagating wave (Hz) and c_f is the sound speed in the fluid (m·s^{-1}).

- ω represents the angular frequency of the propagating wave (rad·s^{-1}). $\omega = 2\pi f$.

- $\boldsymbol{d} \in S^1$ is a unit vector representing the direction of the incident plane wave.

- λ and μ are two positive numbers representing the Lamé coefficients of the considered elastic object Ω^s (Pa).

- ρ_s is a positive number representing the density of the elastic obstacle Ω^s (kg·m^{-3}).

- M^* denotes the adjoint matrix of M. M^* is the complex conjugate of the transpose matrix of M, i.e, $M^* = \overline{M}^t$.

1.2. Mathematical Formulation of the Problem

The time-harmonic scattering problem by an elastic obstacle Ω^s embedded in an infinite homogeneous medium Ω^f can be formulated as the following boundary value problem (BVP):

$$(BVP) \begin{cases} \nabla \cdot \sigma(u) + \omega^2 \rho_s u = 0, & \text{in } \Omega^s, \quad \text{(a)} \\[2ex] \Delta p + k^2 p = 0, & \text{in } \Omega^f, \quad \text{(b)} \\[2ex] \sigma(u) \cdot \nu = -p\nu - p^{inc}\nu, & \text{on } \Gamma, \quad \text{(c)} \\[2ex] \omega^2 \rho_f u \cdot \nu = \frac{\partial p}{\partial \nu} + \frac{\partial p^{inc}}{\partial \nu}, & \text{on } \Gamma, \quad \text{(d)} \\[2ex] \lim\limits_{r \to +\infty} \sqrt{r}\left(\frac{\partial p}{\partial r} - ikp\right) = 0, & \text{(e)} \end{cases} \tag{1}$$

where the pair (u, p) represents the elasto-acoustic scattered field vector; p is the scalar-valued fluid pressure in Ω^f, and $u = (u_x, u_y)^T$ is the vector-valued displacement field in Ω^s; $p^{inc} = e^{i\omega/c_f \boldsymbol{x} \cdot \boldsymbol{d}}$ corresponds to the given incident plane wave. The stress tensor σ is related to the strain tensor ϵ by Hooke's law [44]. Note that this study is limited to the case of an isotropic medium, so that the stiffness tensor is invariant under rotations and reflections [44]. Consequently, we have

$$\sigma(u) = \lambda \nabla \cdot u\boldsymbol{I} + 2\mu\epsilon(u),$$

4

where ϵ is the strain tensor given by

$$\epsilon(u) = \frac{1}{2}\left(\nabla u + (\nabla u)^T\right).$$

Hence, Ω^s is assumed to be a homogeneous scatterer. Observe that the direct problem BVP (1) contains the standard exterior Helmholtz problem given by equations (b) and (e), and the Navier equation given by (a) governing the equilibrium of an elastic scatterer. These equations are coupled via the transmission conditions given by (c) and (d). The first one is a dynamic interface condition whereas the second one is a kinematic interface condition [44]. Furthermore, p_∞, the far-field pattern (FFP) corresponding to the scattered pressure field p, can be expressed using the following integral representation [1]:

$$p_\infty(\hat{\boldsymbol{x}}) = \frac{e^{i\pi/4}}{\sqrt{8\pi k}} \int_\Gamma \left(e^{-ik\hat{\boldsymbol{x}}\cdot\boldsymbol{y}}\frac{\partial p}{\partial \nu}(\boldsymbol{y}) - \frac{\partial e^{-ik\hat{\boldsymbol{x}}\cdot\boldsymbol{y}}}{\partial \nu}p(\boldsymbol{y})\right) dX; \quad \hat{\boldsymbol{x}} \in S^1. \tag{2}$$

Note that BVP has been extensively studied. Mathematical results pertaining to existence, uniqueness, and regularity of the solution can be found in [44, 45, 46, 47, 48, 49], among other references.

1.3. Nondimensionalization of the Forward Problem

The characteristic parameters of a given elastic scatterer Ω^s are of different *nature*. Indeed, it has been reported in [50, 47] that the sensitivity of the FFP given by (2) to changes on the shape Γ is in general quite different to the ones on the material parameters triplet (λ, μ, ρ_s). Such a variability can have, depending on the frequency regime, a dramatic impact on the scattering observability. Furthermore, the magnitude of these parameters is also different. For example, in the numerical experiments reported in Section 5, the Lamé coefficients λ and μ are of order 1 GPa, the density ρ is of order 10^4 kg·m^{-3}, whereas the size of the obstacle is of order 10^{-3}m. Such a difference constitutes a serious numerical challenge when attempting to simultaneously recover these parameters from FFP measurements. Given that, there is undoubtedly a real advantage in *rescaling* the forward problem prior to solving the inverse obstacle problem introduced in Section 1.4. To this end, we proceed in a classical way by rescaling each of the parameters in BVP (1) by a characteristic unit of measure to be determined. Specifically, we introduce the following notation:

$$\hat{v} = \frac{v}{v_0},$$

where v represents one of the parameters $\omega, c_f, \rho_s, \lambda, \mu, u_x, u_y, p$ and v_0 is a characteristic unit of measure v to be determined. In addition, we use a dilation factor L for the position coordinates $\boldsymbol{x} = (x, y)^T$, i.e., $\hat{\boldsymbol{x}} = \frac{1}{L}\boldsymbol{x}$. Furthermore, we assume that $u_{x,0} = u_{y,0} = u_0$. We then rewrite BVP(1) in terms of the new dimensionless quantities $\hat{v}$. We also set all the arising constants to be 1, i.e.,

$$\frac{C_0}{x_0^2\omega_0^2\rho_{s,0}} = \frac{c_{f,0}^2}{L^2\omega_0^2} = \frac{\omega_0^2 u_0\rho_{s,0}L}{p_0} = \frac{C_0 u_0}{Lp_0} = \frac{\omega_0 L}{c_{f,0}} = 1. \tag{3}$$

In doing so, we deduce that $(\hat{u}, \hat{p})$ also satisfies BVP(1) but with dimensionless quantities. Last, we must point out that in all numerical experiments reported in Section 5, we have selected:

- $p_0 = 1$ Pa.

- ω_0 is the angular frequency in each considered numerical experiment.

- $L = L^{(0)}$, where $L^{(0)}$ is the characteristic size of the initial obstacle $\Omega^{s\,(0)}$ selected during the iterative procedure at Stage I for the shape and material parameters recovery.

- $C_0 = \lambda^{(0)} + 2\mu^{(0)}$, where $\lambda^{(0)}$ and $\mu^{(0)}$ are Lamé coefficients of the initial obstacle $\Omega^{s\,(0)}$.

The values of the remaining quantities $\rho_{s,0}, c_{f,0}, u_0$ are then deduced from the relations given by (3).

1.4. The Inverse Problem Formulation

As stated in the Introduction, the main goal of this work is to fully identify elastic scatterers from the knowledge of some corresponding FFP measurements. Therefore, we consider the following inverse obstacle problem (IOP):

Given one or several measured far field patterns $\widetilde{p_\infty}(\hat{\boldsymbol{x}})$ corresponding to one or several given directions $\boldsymbol{d}$ and wavenumbers k of incident plane waves, find Γ the shape of the scatterer Ω^s, its Lamé coefficients (λ, μ), its density ρ_s, and its origin $\boldsymbol{x_c}$ such that

$$F\left(\Gamma, \lambda, \mu, \rho_s, \boldsymbol{x_c}\right)(\hat{\boldsymbol{x}}) = \widetilde{p_\infty}(\hat{\boldsymbol{x}}); \quad \hat{\boldsymbol{x}} \in S \subseteq S^1, \tag{4}$$

where F is the far-field operator that maps $(\Gamma, \lambda, \mu, \rho_s, \boldsymbol{x_c})$ onto the far-field pattern $\widetilde{p_\infty}$.

The tilde notation designates a measured quantity, i.e., a quantity that can be tainted with errors during the measurement process.

To the best of our knowledge, there were no attempts, reported in the literature, to investigate IOP (4), either mathematically or numerically. It is worth noting however that in the case of a rigid obstacle, i.e., Γ being the only unknown in IOP(4), in addition to an extensive numerical investigation (see, e.g.,[1, 8, 22, 21, 9, 11, 51]), various results pertaining to the uniqueness have been established and can be found in [1, 11, 52, 53], among other references.

2. The Proposed Multi-Stage Solution Methodology

As stated earlier in the Introduction, the main goal of this study is to propose an efficient computational procedure for solving IOP(4). The method we have designed is a multi-stage strategy in which a regularized Newton-type algorithm plays a central role. The multi-stage feature of the method is adopted to recognize that the shape, the material parameters, and the origin of the sought-after elastic object, depending on the frequency regime, have different effects on the acoustic scattering observability. More specifically:

- The shape of the scatterer and its material properties are of different nature and scales. Their variations have different influence on the amplitude diffusion of the scattered field, as reported in [50, 47]. Hence, the proposed approach addresses the *scale* issue by considering the non-dimensional formulation (see

Section 1.3) when solving the forward scattering-type problems that occur at each Newton iteration. Furthermore, the different *nature* aspect is addressed through the Tikhonov regularization procedure. Indeed, the choice of the set of the regularization parameters depends on the target parameters, as detailed in Section 3.3.

- It is well-known that, in general, Newton-type methods cannot determine the location of the sought-after object from the knowledge of the phaseless FFP measurements (the FFP modulus measurements). This is due to the fact that the FFP intensity is invariant under translation of the scatterer [53, 1]. On the other hand, it is also well-known that, in practice, FFP intensity measurements are more accurate than the measurements of the phase of the FFP. Hence, since accurate data are very important to ill-posed problems, the proposed method employs phaseless FFP to first recover the shape and the material parameters while keeping the origin of the sought-after obstacle "frozen" at the origin of the plane. Once this stage is completed, the proposed algorithm uses the full FFP measurements to locate the origin of the scatterer.

Next, we examine the algorithmic and computational considerations of the proposed solution methodology and report on its performance when applied to retrieving the parameters of two two-dimensional elastic objects: a non convex octagon made of steel and a mockup submarine made of aluminium. Note that for simplicity purpose, the method is presented in the case where the material parameters are assumed to be constant. The proposed approach can be extended at the formulation level to the case where these parameters depend on the spatial variable x since the characterization of the Fréchet derivatives is possible [50]. However, the numerical aspect is certainly much more challenging. The main challenge lies in finding the appropriate values of the regularization parameters, a critical aspect of the method for convergence and accuracy.

2.1. The Regularized Newton Method

As stated in the Introduction, regularized iterative methods have been among the primary candidates since the mid-80s for solving both two -and three- dimensional scattering problems (see, e.g., [9, 21, 22, 23, 24, 25, 26, 27, 28]). The Newton iterative aspect of these methods addresses effectively the nonlinearity of the IOPs whereas the regularization component is incorporated to restore the stability, as defined by Hadamard in [2]. In what follows, we recall the main features of the regularized Newton method that we employ in the context of the proposed multi-stage solution methodology.

2.1.1. The parametrization

We assume that the sought-after fluid-structure interface Γ can be parametrized as follows:

$$\Gamma = \Gamma(\boldsymbol{s}) \quad ; \quad \boldsymbol{s} = [s_1, ..., s_{N_s}]^T \in \mathbb{R}^{N_s},$$

where N_s denotes the total number of shape parameters s_j. The choice of the parameters depends on the *a priori* knowledge on the shape of the scatterer [9, 1]. We set

$$q = \left[s^T, \lambda, \mu, \rho_s, x_c{}^T\right]^T \in \mathbb{R}^{N_q},$$

where $x_c = (x_c, y_c)^T$, the origin of the scatterer, represents the location of the sought-after scatterer. N_q is the total number of unknown parameters of IOP (4). Hence, $N_q = N_s + 5$.

Since the far-field pattern p_∞ of the scattered pressure field p is measured at a finite number of points $\hat{x}_j \in S^1$, denoted by $N_{\hat{x}}$, we project IOP (4) onto a finite dimensional space of $L^2(S^1)$, which is the natural choice for the measurements' space, and transform it onto the following algebraic problem:

$$\begin{cases} \text{Find } q \in \mathbb{R}^{N_q} \text{ such that} \\ F\left(q\right)(\hat{x}_j) = \widetilde{p_\infty}(\hat{x}_j); \quad j = 1, ..., N_{\hat{x}}. \end{cases} \tag{5}$$

Observe that the resulting inverse problem given by (5) is a discrete formulation of IOP (4). It is a nonlinear algebraic system with $N_{\hat{x}}$ equations and N_q unknowns; $N_{\hat{x}}$ being larger than N_q when reconstructing with full aperture measurements. The finite-dimensional inverse problem given by (5) is a *discrete* formulation of IOP(4). It is a nonlinear algebraic system with $N_{\hat{x}}$ equations and N_p unknowns. Note that this system can also be formulated as an (unconstrained) optimization problem, and that its solution **p** can also be defined by

$$\mathbf{q} = \arg \min_{\mathbf{p} \in \mathbf{R}^{N_q}} \left\| \begin{array}{c} [F(\Gamma(\mathbf{p}))](\hat{x}_1) - \widetilde{\mathbf{p}}_\infty(\hat{x}_1) \\ \vdots \\ [F(\Gamma(\mathbf{p}))](\hat{x}_{N_{\hat{x}}}) - \widetilde{\mathbf{p}}_\infty(\hat{x}_{N_{\hat{x}}}) \end{array} \right\|_2, \tag{6}$$

where arg is used to denote that **q** is the minimizer of the considered vector function over $\mathbf{R}^{N_q}$

2.1.2. The regularized Newton equation using full FFP measurements

The solution of the nonlinear inverse problem IOP (5) by the Newton method incurs, at each Newton iteration n, the solution of the following linear algebraic system:

$$J_F\left(q^{(n)}\right) \delta q^{(n)} = \widetilde{\mathbf{p}_\infty} - \mathbf{p}_\infty^{(n)}, \tag{7}$$

where

- $J_F\left(q^{(n)}\right)$ is the $N_{\hat{x}} \times N_q$ Jacobian matrix of the operator F.

- $\widetilde{\mathbf{p}_\infty}$ is the FFP measurements vector, that is,

$$\widetilde{p_\infty} = [\widetilde{p_\infty}(\hat{x}_1), ..., \widetilde{p_\infty}(\hat{x}_{N_{\hat{x}}})]^T.$$

- $p_\infty^{(n)}$ is the FFP computed vector at iteration n, that is,

$$p_\infty^{(n)} = \left[p_\infty^{(n)}(\hat{x}_1), ..., p_\infty^{(n)}(\hat{x}_{N_{\hat{x}}})\right]^T.$$

8

Once the vector $\boldsymbol{\delta q}^{(n)} \in \mathbb{R}^{N_q}$ is calculated, the value of the sought-after parameter vector is then updated as follows:

$$q^{(n+1)} = q^{(n)} + \boldsymbol{\delta q}^{(n)}. \tag{8}$$

Moreover, since in practice the number of observation points $N_{\hat{x}}$ is greater than the number of the parameters N_q, the linear system (7) is overdetermined. Therefore, it is solved in the least-squares sense. Hence, the linear system given by (7) is replaced by the following corresponding *normal* equations:

$$J_F^* \left(q^{(n)} \right) J_F \left(q^{(n)} \right) \boldsymbol{\delta q}^{(n)} = J_F^* \left(q^{(n)} \right) \left(\widetilde{p_\infty} - p_\infty^{(n)} \right). \tag{9}$$

Due to the ill-posedness nature of IOP (4), the discrete linear system (9) is severely ill-conditioned. This means that small perturbations in the data may lead to large changes in the solution. For this reason, a regularization procedure must be incorporated into (9) to address the lack of stability [54, 55]. We propose a Tikhonov-based strategy to restore the stability to the linear system (9) [56, 57]. This consists in replacing (9) by the following *regularized* system:

$$\left(J_F^* \left(q^{(n)} \right) J_F \left(q^{(n)} \right) + \mathfrak{R}^{(n)} \right) \boldsymbol{\delta q}^{(n)} = J_F^* \left(q^{(n)} \right) \left(\widetilde{p_\infty} - p_\infty^{(n)} \right), \tag{10}$$

where $\mathfrak{R}^{(n)}$ is a $N_q \times N_q$ *diagonal* and positive definite matrix, called the regularization matrix. The selection of the diagonal entries of $\mathfrak{R}^{(n)}$ is discussed in Section 3.3. Note that (10) is used in Stage II of the proposed algorithm to retrieve the location of the scatterer. Therefore, the unknown parameters vector **q** is in fact a vector in R^2 whose entries are the coordinates of the scatterer's location, i.e., $\mathbf{q} = \mathbf{q_{II}} = [x_1, x_2]^T$.

2.1.3. The regularized Newton equation using phaseless FFP measurements

It is well-known that in practice the FFP intensity measurements are obtained with higher accuracy level than the corresponding phase measurements. In addition, accurate data are very important to ill-posed problems. Note that it is possible to reconstruct both the shape and the material parameters using the full FFP measurements, as reported in [30]. Therefore, we propose to use these reduced FFP data when retrieving the parameters s, λ, μ, and ρ_s. Note that the intensity of the FFP is defined here as the *square* of the amplitude of the FFP:

$$U \left(q^{(n)} \right) (\hat{\boldsymbol{x}}_j) = \overline{F \left(q^{(n)} \right) (\hat{\boldsymbol{x}}_j)} F \left(q^{(n)} \right) (\hat{\boldsymbol{x}}_j) = \mid p_\infty^{(n)}(\hat{\boldsymbol{x}}_j) \mid^2; \quad j = 1, ..., N_{\hat{x}}.$$

Consequently, the computation of the vector $\boldsymbol{\delta q}^{(n)}$ needed in (8) is obtained by solving the following regularized least-squares system:

$$\left(J_U^* \left(q^{(n)} \right) J_U \left(q^{(n)} \right) + \mathfrak{R}^{(n)} \right) \boldsymbol{\delta q}^{(n)} = J_U^* \left(q^{(n)} \right) \left(\widetilde{U} - U \left(q^{(n)} \right) \right), \tag{11}$$

where $J_U(q^{(n)})$ is the Jacobian matrix corresponding to the intensity operator $U(q^{(n)})$. It is given by

$$J_U \left(q^{(n)} \right) = 2\mathcal{R}e \left[\overline{F(q^{(n)})}^T J_F(q^{(n)}) \right], \tag{12}$$

9

where $\mathcal{R}e$ designates the real part of a complex valued quantity and $\widetilde{U}$ denotes the measured intensity vector. It is defined by

$$\widetilde{U} = \left[|\ \widetilde{\boldsymbol{p_\infty}}(\hat{\boldsymbol{x}}_1)\ |^2, ..., |\ \widetilde{\boldsymbol{p_\infty}}(\hat{\boldsymbol{x}}_{N_{\hat{x}}})\ |^2 \right]^T .$$

Furthermore, the vector $\boldsymbol{U}\left(\boldsymbol{q}^{(n)}\right)$ is the computed intensity vector at iteration n. It is given by

$$\boldsymbol{U}\left(\boldsymbol{q}^{(n)}\right) = \left[U\left(\boldsymbol{q}^{(n)}\right)(\hat{\boldsymbol{x}}_1), ..., U\left(\boldsymbol{q}^{(n)}\right)(\hat{\boldsymbol{x}}_{N_{\hat{x}}}) \right]^T .$$

We must point out that, in general, it is not possible to retrieve the location of the sought-after scatterer given by $\boldsymbol{x_c}$ from the knowledge of its corresponding FFP intensity. This is due to the fact that the FFP intensity operator is *invariant* under translations of the scatterer Ω^s (see, e.g., [1, 53, 36] or Appendix D, pp. 207–208 in [50]). For this reason, the linear system (8) and (11) will only be employed to recover the shape and the material parameters of Ω^s. Therefore, the unknown parameters vector $\mathbf{q}$ used in (11) is in fact a vector in $R^{N_{\hat{x}}+3}$ whose entries are the shape parameters and the material parameters, i.e., $\mathbf{q} = \mathbf{q_I} = [\mathbf{s}, \lambda, \mu, \rho_s]^T$.

2.2. The Multi-Stage Solution Procedure

The proposed solution method is a multi-stage procedure in which the regularized Newton algorithm given by (8)-(10) or (8)-(11) is its corner stone. The proposed method recognizes that the sought-after parameters have different influence on the scattering observability and can be described as follows:

Stage 0. We initiate the algorithm by selecting an arbitrary value of the initial vector parameter $\boldsymbol{q}^{(0)}$.

Stage I. This stage is devoted to the simultaneous recovery of the shape and material parameters $\mathbf{q} = \mathbf{q_I} = [\mathbf{s}, \lambda, \mu, \rho_s]^T$. This is accomplished by iterating the regularized Newton system (11) and (8).

Stage II. This stage is dedicated to the determination of the origin $\mathbf{q} = \mathbf{q_{II}} = x_1, x_2]^T$ of the elastic scatterer computed in Stage I. This goal is achieved by iterating the regularized Newton system (10) and (8).

3. The Computational Requirements

We describe in this section the three critical computational requirements of the algorithm: the evaluation of the Jacobians, the solution of the forward problem, and the selection of the regularization matrix entries.

3.1. Effective Evaluation of the Jacobians

As indicated in (10) and (11), a key step for employing the proposed multi-stage strategy is the computation, at each Newton iteration n, of the $N_{\hat{x}} \times N_{\boldsymbol{q}}$ entries of the Jacobian matrix $J_F(\boldsymbol{q}^{(n)})$. Such calculations must be performed efficiently and with a high accuracy level to ensure stability, fast convergence, and cost effectiveness of the proposed computational procedure. To this end, we exploit the mathematical results

pertaining to the dependence of the operator F with respect to the domain [58, 48] and to the material parameters [50, 47]. The results established in [58] state that the operator F is continuously differentiable with respect to the domain Ω^s. This result has been established assuming the domain Ω^s to be Lipschitz continuous. Moreover, the result reported in [48] provides a characterization of the derivative of F with respect to the boundary of Ω^s, that is of practical computational interest. The proof of the result assumes Ω^s to be a Lipschitz continuous polygonal domain. Furthermore, the results established in [50, 47] prove that F is also continuous differentiable with respect to the material parameters and provide a characterization of its corresponding derivatives. More specifically, let $p_l'^{(n)}$ (resp. $u_l'^{(n)}$) be the derivative of the pressure field p (resp. displacement field u) in the direction of a considered parameter q_l; $l = 1, ..., N_{\boldsymbol{q}}$ at iteration n, i.e., corresponding to the configuration $\Omega^s(\boldsymbol{q}^{(n)})$. Then, the pair $(p_l'^{(n)}, u_l'^{(n)})$ is the solution of the following elasto-acoustic scattering-type problem:

$$(BVP) \begin{cases} \nabla \cdot \sigma(u_l'^{(n)}) + \omega^2 \rho_s u_l'^{(n)} = f_1^{(n)}, & \text{in } \Omega^{s(n)}, \quad \text{(a)} \\[2mm] \Delta p_l'^{(n)} + k^2 p_l'^{(n)} = f_2^{(n)}, & \text{in } \Omega_b^{f(n)}, \quad \text{(b)} \\[2mm] \sigma(u_l'^{(n)}) \cdot \nu + p_l'^{(n)} \nu = g_1^{(n)}, & \text{on } \Gamma^{(n)}, \quad \text{(c)} \\[2mm] \omega^2 \rho_f u_l'^{(n)} \cdot \nu - \frac{\partial p_l'^{(n)}}{\partial \nu} = g_2^{(n)}, & \text{on } \Gamma^{(n)}, \quad \text{(d)} \\[2mm] \lim_{r \to +\infty} \sqrt{r} \left(\frac{\partial p_l'^{(n)}}{\partial r} - ik p_l'^{(n)} \right) = 0, & \text{(e)} \end{cases} \tag{13}$$

where $f_1^{(n)}, f_2^{(n)}, g_1^{(n)}$ and $g_2^{(n)}$ are functions whose expressions depend on the nature of the parameter q_l. More specifically:

- If q_l is a shape or a position parameter, then $f_1^{(n)} = f_2^{(n)} = 0$,

$$g_1^{(n)} = -h_j^t \nabla \sigma(u^{(n)}) \nu - \nabla(p^{(n)T} \cdot h_j^{(n)} \nu + \sigma(u^{(n)})[h_j']^t \nu + (p^{(n)T}[h_j']^t \nu,$$

  and

$$g_2^{(n)} = -(\omega^2 \rho_f \nabla u^{(n)} - \nabla(\nabla(p^{(n)T})) h_j \cdot \nu + (\omega^2 \rho_f u^{(n)} - \nabla(p^{(n)T})) \cdot [h_j']^t \nu,$$

  where

$$h_l^{(n)} = \frac{\partial \Gamma}{\partial q_l}(\boldsymbol{q}^{(n)}).$$

- If q_l is the Lamé coefficient λ, then $f_2^{(n)} = g_2^{(n)} = 0$ and we have

$$f_1^{(n)} = -\nabla \cdot \left(\nabla \cdot u^{(n)} \boldsymbol{I} \right) \text{ and } g_1^{(n)} = - \left(\nabla \cdot u^{(n)} \boldsymbol{I} \right) \cdot \nu.$$

11

- If q_l is the Lamé coefficient μ, then $f_2^{(n)} = g_2^{(n)} = 0$ and we have

$$f_1^{(n)} = -2\,\nabla \cdot \epsilon(u^{(n)}) \text{ and } g_1^{(n)} = -2\,\epsilon(u^{(n)}) \cdot \nu.$$

- If q_l is the density coefficient ρ, then $f_2^{(n)} = 0$; $g_1^{(n)} = g_2^{(n)} = 0$ and we have

$$f_1^{(n)} = -\omega^2 u^{(n)}.$$

Once the derivatives $p_l'^{(n)}$ and $u_l'^{(n)}$ are evaluated, the "far-field pattern" $p_{l,\infty}'^{(n)}$, at iteration n, is then post-processed using the integral representation given by (2) with $p_l'^{(n)}$ and $\Gamma^{(n)}$. Consequently, we deduce the entries of the Jacobian matrix $J_F(\boldsymbol{q}^{(n)})$ as follows:

$$J_F(\boldsymbol{q}^{(n)})_{lj} = p_{l,\infty}'^{(n)}(\hat{x}_j); \quad j = 1, ..., N_{\hat{x}}; \quad l = 1, ..., N_{\boldsymbol{q}}.$$

Hence, it follows that, at each regularized Newton iteration n, the Jacobian matrix $J_F(\boldsymbol{q}^{(n)})$ can be computed by solving $N_{\boldsymbol{q}}$ direct elasto-acoustic scattering-type problems that differ only by additional terms in the right-hand sides of transmission conditions and/or in the wave equations. This means that, at the algebraic level (that results from any finite element-type discretization [59]), the matrix entries of $J_F(\boldsymbol{q}^{(n)})$ are obtained by solving a single linear system with multiple right-hand sides.

Remark 1. We must point out that employing adjoint-based formulations could be an attractive alternative for solving inverse obstacle elasto-acoustic problems. One of the main advantages of this class of methods is that the derivatives are expressed for all perturbations, which makes this class of methods independent of the number of the shape parameters. In addition, these methods require solving one forward problem and its corresponding adjoint problem. However, since the resulting linear system corresponding to the direct problem is symmetric but not Hermitian, its factorization cannot be reusable to solve the adjoint problem. Hence, the computational cost associated with the assembly and the factorization of two linear systems could be superior to the one required for the solution of one linear system with multiple right-hand sides.

3.2. Solving Efficiently the Forward Problem

At each iteration n, the regularized Newton system (see (10) and (11)) calls for the solution of the elasto-acoustic scattering problem BVP(1) and BVP(13). Although these problems are linear in nature, their numerical solutions are notoriously difficult due mainly to the following two reasons: (a) they are set in an unbounded (infinite) domain and (b) the scattered field is highly oscillatory (for high frequency regime).

To address the unboundness aspect, we propose to reformulate BVPs (1) and (13) in a bounded domain Ω_Σ^f, by surrounding the scatterer Ω^s with an artificial boundary Σ (see Fig. 1). The Sommerfeld condition (see (e) of BVPs (1) and (13)) is then replaced by the following exterior boundary condition of first order, in the sense of the pseudo-differential framework adopted in [60]:

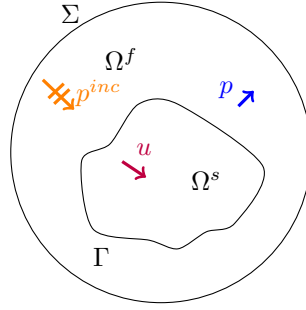$$\frac{\partial p}{\partial \nu} = ikp - \frac{\kappa}{2}p, \qquad \text{on } \Sigma, \tag{14}$$

12

Figure 1: Schematic description of the problem statement in a finite domain.

where κ denotes the curvature of Σ. Since we have chosen Σ to be a circle of radius R, then $\kappa = \frac{1}{R}$. We have chosen this Robin-type boundary condition for mainly the following two considerations: (a) its computational simplicity and (b) its performance efficiency. Indeed, the approximation of the boundary condition (14) by a finite element method introduces only additional mass-like matrices defined on the exterior boundary Σ. Building these matrices is straightforward. Moreover, when compared to a second-order absorbing boundary condition [61] or to a perfectly matched layer (PML) condition [62], it has been reported in [63] that the first-order absorbing boundary condition (14) exhibits a comparable accuracy level, if not better, when employed in the low- and mid- frequency regime, i.e., the frequency band considered in this paper. Needless to say that one may use higher order absorbing boundary condition when performing these calculations in high frequency regime.

Once the direct scattering problems BVP (1) and BVP (13) are formulated in a bounded domain Ω_Σ^f, we solve them numerically using the interior penalty discontinuous Galerkin (IPDG) method introduced in [64]. The proposed IPDG method possesses two distinctive features. First, it employs high-order polynomial functions to ensure an accurate approximation of highly oscillating waves. Second, it is equipped with curved boundary edges to provide an accurate representation of the fluid-structure interface Γ. The importance of an accurate representation of Γ has been demonstrated by the numerical results reported in [64]. These results indicate that (a) there is an improvement on the accuracy level by -at least- two orders of magnitude and (b) unlike when approximating Γ by a "broken" line, there are no more spurious internal resonances in the fluid region.

The IPDG formulation can be expressed, at the algebraic level, as follows [64]:

$$\begin{pmatrix} \boldsymbol{A^f} + \boldsymbol{C} & \boldsymbol{B} \\ \boldsymbol{B^*} & \boldsymbol{A^s} \end{pmatrix} \begin{pmatrix} P \\ U \end{pmatrix} = \begin{pmatrix} F_1 \\ F_2 \end{pmatrix},$$ (15)

where $\boldsymbol{A^f}$ and $\boldsymbol{A^s}$ are symmetric matrices given by:

$$\boldsymbol{A^f} = \frac{1}{\omega^2}(\boldsymbol{K^f} - k^2 \boldsymbol{M^f} - \boldsymbol{J^f} + \boldsymbol{S^f}),$$

13

and

$$\boldsymbol{A^s} = \boldsymbol{K^s} - \omega^2 \rho_s \, \boldsymbol{M^s} - \boldsymbol{J^s} + \boldsymbol{S^s},$$

where

- $\boldsymbol{K^f}$ (resp. $\boldsymbol{K^s}$) is the stiffness matrix associated to the pressure (resp. the displacement) field.

- $\boldsymbol{M^f}$ (resp. $\boldsymbol{M^s}$) is a block diagonal mass matrix associated to the pressure (resp. the displacement) field.

- $\boldsymbol{J^f}$ (resp. $\boldsymbol{J^s}$) is a matrix that contains the jump terms. The entries of this matrix are defined over the interior edges in the fluid (resp. in the solid).

- $\boldsymbol{S^f}$ (resp. $\boldsymbol{S^s}$) is a block-diagonal mass-like matrix defined over the interior edges in the fluid (resp. the solid) resulting from the penalty term.

The matrix $\boldsymbol{C}$ is the complex-valued damping matrix. It is a mass-like matrix whose entries are all zeros except for the elements located at the exterior boundary Σ. The matrix $\boldsymbol{A^f} + \boldsymbol{C}$ is symmetric but non-hermitian, and thus not positive-definite. Note that the interior penalty term compensates the weak ellipticity of the equation operator. Hence, $\boldsymbol{A^s}$ is positive-definite up to the Jones frequencies [49, 45]. The matrix $\boldsymbol{B}$ is a mass-like boundary matrix whose entries are defined on the interface edges only, whereas F_1 and F_2 are the source vectors. The vector P (resp. U) is the fluid pressure (resp. structural displacement) representation in the finite element basis.

The linear system given by (15) is thus composed of sparse matrices whose symmetry property allows for an optimized storage. This system is solved with the LU factorization procedure developed for sparse systems and incorporated in the open-source program suite MUMPS [65, 66]. Note that, in the low- and mid-frequency regimes, the sparse implementation allows for running the numerical experiments on a personal computer.

Last, as stated in Section 3.1, the Fréchet derivative of the elasto-acoustic scattered field with respect to the parameter q_j can be evaluated at each iteration by solving the same linear system (15), but with different right-hand sides.

3.3. Computation of the regularization matrix $\mathfrak{R}^{(n)}$

It is well-known that the convergence of any regularized iterative algorithm highly depends on the choice of the regularization procedure. For this reason, various strategies have been developed for selecting "optimal" regularization values [67, 68, 69, 70]. However, all these strategies have been designed based on theoretical considerations that unfortunately are limited to linear problems. Given that, we propose to employ a trial and error strategy for selecting, at each Newton iteration, the diagonal entries of the regularization matrix $\mathfrak{R}^{(n)}$. Such a choice is a balance act between the stability of the algorithm and its accuracy. Note that the proposed "brute force" approach recognizes the different influences of the sought-after parameters on the scattering observability. This is why the choice of the entries of $\mathfrak{R}^{(n)}$ depends on the algorithm stage.

14

In what follows, we provide a succinct description on how to select the regularization matrix $\mathfrak{R}^{(n)}$ in each stage of the proposed iterative algorithm.

3.3.1. The choice of $\mathfrak{R}^{(n)}$ in Stage I

We first recall that Stage I is dedicated to the simultaneous search of the shape parameter vector $\boldsymbol{s} \in \mathbb{R}^{N_s}$ and the material parameter triplet $(\lambda, \mu, \rho_s) \in \mathbb{R}^3$. In this case, the regularization matrix $\mathfrak{R}^{(n)}$ is a *diagonal* matrix whose $N_{\boldsymbol{s}} + 3$ diagonal entries $\mathfrak{R}_{ll}^{(n)}$ are given by

$$
\mathfrak{R}_{ll}^{(n)} = \begin{cases}
\alpha_s^{(n)} & ; & 1 \leq l \leq N_s, \\
\alpha_p^{(n)} & ; & N_s + 1 \leq l \leq N_s + 2, \\
\alpha_{\rho_s}^{(n)} & ; & l = N_s + 3,
\end{cases}
$$

where the regularization parameters $\alpha_s^{(n)}, \alpha_p^{(n)}$ and $\alpha_{\rho_s}^{(n)}$ are positive numbers.

At each iteration n, the "optimal" value of the triplet $(\alpha_s^{(n)}, \alpha_p^{(n)}, \alpha_{\rho_s}^{(n)})$ is obtained by sweeping each of the three regularization parameters over a large interval of positive numbers and evaluating the corresponding *residuals*, i.e., the relative errors, in the euclidean norm in $\mathbb{R}^{N_{\hat{x}}}$, between the measured FFP intensity vector $\widetilde{\boldsymbol{U}}$ and the computed one $U\left(\boldsymbol{q}^{(n)}\right)$, and then selecting the value of the triplet that leads to the minimum residual (up to the noise level in the data), i.e., the convergence of the algorithm. Note that we also monitor, at the same time, the relative errors between two successive solutions $\boldsymbol{q}^{(n)}$ and $\boldsymbol{q}^{(n+1)}$ to determine whether or not the algorithm is stagnating, i.e., the algorithm is "trapped" at local minimum. Note that stagnation occurs when the successive relative difference on the computed parameters is lower than a prescribed tolerance and in the same time the relative residual values are still above the prescribed accuracy level dictated by the noise level in the measurements. In all the numerical experiments reported in Section 5, we have set this tolerance to be 0.1. Furthermore, we must point out that the proposed brute force approach for selecting, at each iteration, the "optimal" value of the regularization triplet is actually not a systematic three dimensional sweeping procedure that leads to a prohibitive computational cost. The proposed strategy consists in tracking the "optimal" value along a one-dimensional curve. Indeed, after an appropriate initialization, we proceed in three steps. In each step, we vary the values of one regularization parameter while the values of the two others remain "frozen". More specifically, we proceed as follows:

- **Initialization: selecting an initial guess.** All three regularization parameters are chosen to be two order of magnitude greater than the largest diagonal entries of the normal system in (11), i.e., we set:

$$
\alpha_s^{(0)} = \alpha_p^{(0)} = \alpha_{\rho_s}^{(0)} = 10^2 \max_{1 \leq l \leq N_{\boldsymbol{s}}+3} \left(J_U^* \left(\boldsymbol{q}^{(0)}\right) J_U \left(\boldsymbol{q}^{(0)}\right) \right)_{ll}.
$$

- **Step 1: Varying $\alpha_s^{(n)}$ only.** We start running the algorithm using the regularization matrix $\mathfrak{R}^{(0)}$. At each iteration, we evaluate the relative residual and the successive relative error. If stagnation occurs and/or the relative residual increases, then the value of $\alpha_s^{(n)}$ is reduced while the values of the two others remain unchanged, i.e., $\alpha_p^{(n)} = \alpha_p^{(0)}$ and $\alpha_{\rho_s}^{(n)} = \alpha_{\rho_s}^{(0)}$.

15

A typical reduction factor of $\alpha_s^{(n)}$ employed in the experiments reported in Section 5 is $1/10$. We continue iterating the algorithm and decreasing $\alpha_s^{(n)}$ until either the corresponding FFP intensity residual reaches the noise level or stagnation occurs. At stagnation, we go to Step 2.

We must point out that we have observed, as anticipated, that only the sequence of the shape parameter vector $\boldsymbol{s}^{(n)}$ tends to converge, in this step, to the sought-after parameter $\boldsymbol{s}$.

- **Step 2: Varying $\alpha_p^{(n)}$ only.** This step is similar to Step 1. The only difference is that here the value of $\alpha_p^{(n)}$ varies whereas $\alpha_s^{(n)}$ remains frozen. Indeed, in this step, the value of $\alpha_{\rho_s}^{(n)}$ is still the initial value, i.e., $\alpha_{\rho_s}^{(n)} = \alpha_{\rho_s}^{(0)}$ and the value of $\alpha_s^{(n)}$ is set to be the last selected value in Step 1. We iterate the algorithm and decrease the value of $\alpha_p^{(n)}$ at each stagnation or oscillation of the relative residual. We continue until the FFP residuals reach the noise level or the algorithm stagnates. If stagnation occurs, we go to Step 3. Similarly to Step 1, we have observed that at the end of this step, the sequence of material parameters $(\lambda^{(n)}, \mu^{(n)})$ tends to converge to the target parameter values (λ, μ).

- **Step 3: Varying $\alpha_{\rho_s}^{(n)}$ only.** We repeat exactly the same process described in Step 1 and Step 2. The only difference is that in this step, we decrease the value of $\alpha_{\rho_s}^{(n)}$ while setting the value of $\alpha_s^{(n)}$ (resp. $\alpha_p^{(n)}$) to be the last value selected in Step 1 (resp. Step 2). Note that at the end of Step 3, the density sequence $\rho_s^{(n)}$ tends to converge to the target value ρ_s.

We must point out that in the event that the relative residual value does not reach the noise level, we repeat the full process starting with an initial guess for each parameter being the latest value selected at each corresponding step and using FFP measurements corresponding to a higher wavenumber k.

Remark 2. The main motivation for selecting a unique regularization parameter for the Lamé coefficients is to use the smallest possible number of regularization parameters for two practical reasons. First, we observed that when solving this inverse problem and determining the Lamé coefficients only, that is, we assume that the shape and the location of the scatterer along with its density are known, there was not need to use more than one regularization parameter for successfully recovering these parameters [50]. Second, in the absence of theoretical results on the choice of the regularization parameters optimal values, their determination is accomplished via a trial and error strategy. Hence, involving a number of parameters larger than three will quickly make the process of selecting these values extremely challenging (if not impossible!) and most likely computationally prohibitive.

3.3.2. The Choice of $\mathfrak{R}^{(n)}$ in Stage II

We recall that Stage II is dedicated to the determination of the origin of the scatterer $\boldsymbol{x_c} = (x_c, y_c)$ using the regularized Newton equation given by (8) and (10). In this case, the regularization matrix $\mathfrak{R}^{(n)}$ is a diagonal matrix given by

$$\mathfrak{R}^{(n)} = \alpha_c^{(n)} \boldsymbol{I},$$

where $\boldsymbol{I}$ is the 2×2 identity matrix and $\alpha_c^{(n)}$ is a positive number representing the regularization parameter. Due to the small size of the linear system (10), the trial and error strategy for finding the optimal value of $\alpha_c^{(n)}$ is simpler and "cheaper" than in Stage I.

4. Algorithm Summary and Computational Complexity

The description of the proposed solution methodology is summarized in this section along with the required calculations that affect the complexity and the computational cost for its implementation.

4.1. Algorithm Summary

The proposed multi-stage solution methodology for solving the inverse problem IOP(4) can be summarized as follows.

Stage 0: Initialization. The following initial data are required:

- A measured set of FFP, for one or several frequencies, at some observation points $\hat{\boldsymbol{x}}_1, ..., \hat{\boldsymbol{x}}_{N_{\hat{x}}}$, i.e., the FFP vector

$$\widetilde{\boldsymbol{p_\infty}} = [\widetilde{p_\infty}(\hat{\boldsymbol{x}}_1), ..., \widetilde{p_\infty}(\hat{\boldsymbol{x}}_{N_{\hat{x}}})]^T \in \mathbb{C}^{N_{\hat{x}}},$$

and its corresponding intensity

$$\widetilde{\boldsymbol{U}} = \left[| \widetilde{\boldsymbol{p_\infty}}(\hat{\boldsymbol{x}}_1) |^2, ..., | \widetilde{\boldsymbol{p_\infty}}(\hat{\boldsymbol{x}}_{N_{\hat{x}}}) |^2\right]^T \in \mathbb{R}^{N_{\hat{x}}}.$$

The tilde indicates that these measurements are tainted with a *known* noise level.

- An initial parameter vector $\boldsymbol{q}^{(0)} = \left[\boldsymbol{s}^{(0)}, \lambda^{(0)}, \mu^{(0)}, \rho_s^{(0)}\right]^T \in \mathbb{R}^{N_s+3}$. The coordinates of the vector $\boldsymbol{q}^{(0)}$ are selected arbitrarily, i.e., $\boldsymbol{q}^{(0)}$ is a "blind" guess. Note that the initial origin $\boldsymbol{x_c}^{(0)}$ of the scatterer is typically set to be the origin of the plane, that is, $\boldsymbol{x_c}^{(0)} = (0,0)^T$.

We then construct the initial domain $\Omega_s^{(0)}$ and solve BVP(1) to deduce the FFP $p_\infty^{(0)}$ and its corresponding intensity $U^{(0)}$.

Stage I: Retrieving simultaneously the shape and material parameters $\boldsymbol{q} = [\boldsymbol{s}, \lambda, \mu, \rho_s]^T$. For a given frequency, this stage requires accomplishing successively the following tasks:

- The construction, at each iteration n, of the Jacobian matrix $J_U(\boldsymbol{q}^{(n)})$ given by (12).

- The application of the regularized Newton algorithm given by (8) and (11) until either the FFP residual reaches the noise level or a stagnation occurs.

  Note that the regularization matrix $\mathfrak{R}^{(n)}$ is selected according to the guidelines provided in Section 3.3.1. Moreover, at each iteration n, the intensity field $\boldsymbol{U}(\boldsymbol{q}^{(n)})$ must be computed to monitor the algorithm convergence. If stagnation occurs, we switch to a higher wavenumber k and repeat the procedure described in Stage 1 with an initial guess $\boldsymbol{q}^{(0)}$ being the computed value $\boldsymbol{q}^{(n)}$ at the stagnated iteration.

17

Stage II: Recovering the origin parameters, i.e., $\boldsymbol{q} = [x_c, y_c]^T$. The initial guess at this stage is $\boldsymbol{q}^{(0)} = [0,0]^T$ and the initial shape and material parameters correspond to the computed parameters $\left[\boldsymbol{s}^{(n)}, \lambda^{(n)}, \mu^{(n)}, \rho_s^{(n)}\right]^T$ at convergence in Stage 1. This stage requires accomplishing successively the following two tasks:

- The construction, at each iteration n, of the Jacobian matrix $J_F(\boldsymbol{q}^{(n)})$ defined in Section 2.1.2.

- The application of the regularized Newton algorithm given by (8) and (10) until either the FFP residual attains the noise level or a stagnation occurs. The regularization matrix $\mathfrak{R}^{(n)}$ is selected according to the procedure described in Section 3.3.2. Note that we switch to a higher frequency if the algorithm stagnates.

4.2. Computational Complexity

The proposed multi-stage procedure for solving IOP (4) mainly requires, for a given frequency, the following calculations.

Stage 0. Only one sparse linear system that results from the IPDG-discretization of BVP(6) (see section 3.2) needs to be solved. This is accomplished using an LU factorization, as indicated in Section 3.2.

Stage I. Two linear systems are solved. These are:

- The sparse linear system given by (15) with $N_{\boldsymbol{s}} + 3$ different right-hand sides in order to determine the entries of the Jacobian matrix.

- The linear system given by (11) to determine the update $\boldsymbol{\delta q}^{(n)}$. This is accomplished, for each selected regularization matrix (see Section 3.3.1), using LU-factorization.

Stage II. Two linear systems need also to be solved. These are:

- The sparse linear system (15) with two different right-hand sides in order to determine the entries of the Jacobian matrix.

- A 2×2 linear system given by (10) to determine the update $\boldsymbol{\delta q}^{(n)}$. This is accomplished for each selected regularized parameter α_c (see Section 3.3.2), using an analytical inversion.

5. Performance Assessment: Numerical Investigation

We investigate the convergence and the accuracy of the proposed multi-stage solution methodology, as well as its robustness to the noise level in the measurements. To this end, we consider synthetic FFP measurements corresponding to a single incident direction $\vec{d} = (1,0)$ but for one or multiple frequencies. The measured data are obtained by sampling the full aperture of the FFP at 360 points. They are contaminated with white noise of levels ranging from 0% to 15% to mimic possible errors in the measurements. Note that the noise level is measured in the sense of the Euclidean norm. In what follows, we report on the

determination of the values of the parameters characterizing two non-convex elastic scatterers: (a) a non-convex octagon and (b) a mockup-submarine. Note that the first scatterer is made of *steel*, whereas the second one is made of *aluminum*.

We first analyze the performance of the algorithm when the synthetic measurements are noise-free. We then investigate its sensitivity to the noise level. Last, we present results to illustrate the importance of using multiple frequencies to improve both the convergence and the accuracy of the inversion procedure, particularly when retrieving the material parameters. More numerical identification results are reported in [71], which can be found in the Hal repository, a multi-disciplinary open-access archive for the deposit and dissemination of scientific research documents, whether they are published or not.

We must point out that this numerical investigation considers three scenarios of practical interest. First, we focus on parameter identification problems or detailed design problems where the shape of the elastic scatterer is known in some general sense but its size and the size of its features are unknown. Then, we consider a blind problem situation where the target obstacle cannot be described by the shape parametrization adopted for representing the trial solutions. Last, we consider an other category of blind problems where little if any specific information about the shape of the target and therefore for which as general as possible a parametrization is warranted.

5.1. Performance analysis in the absence of noise

We analyze in this section the performance efficiency of the proposed computational procedure when using noise-free synthetic FFP measurements. We will conduct this investigation by focusing on parameter identification problems or detailed design problems where the shape of the elastic scatterer is known in some general sense. In this particualr scenario, it is known that the target obstacle is an octagon or a mockup submarine but its size and the size of its features are unknown.

5.1.1. Case of an octogonal-shaped domain

In this experiment, we determine the characteristic parameter values of a non-convex octagon elastic scatterer Ω^s immersed in water Ω^f (see Fig. 2(a)). The sought-after scatterer Ω^s is made of *steel* and its wet boundary Γ is represented by the following piecewise linear parametrization:

$$\Gamma = \left\{ (x_c, y_c)^T + \sum_{j=1}^{8} (1-t)X_j + tX_{j+1} \quad ; \quad t \in [0,1] \right\}, \tag{16}$$

where the vertices X_j are given by:

$$X_j = s_j \begin{pmatrix} \cos \theta_j \\ \sin \theta_j \end{pmatrix} \quad ; \qquad j = 1, ..., 8.$$

Note that the vertices are uniformly distributed in the polar coordinate angle. The values of the shape parameters s_j together with the center of the scatterer (x_c, y_c), as well as the material parameters (λ, μ, ρ) are reported in Fig. 3.
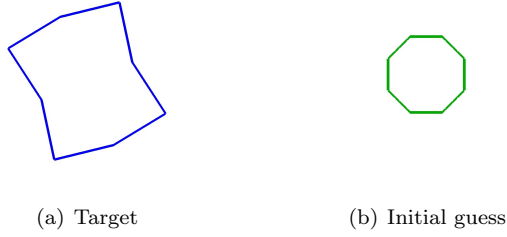
19

(a) Target   (b) Initial guess

Figure 2: Octogonal scatterers. Target vs. Initial Guess.

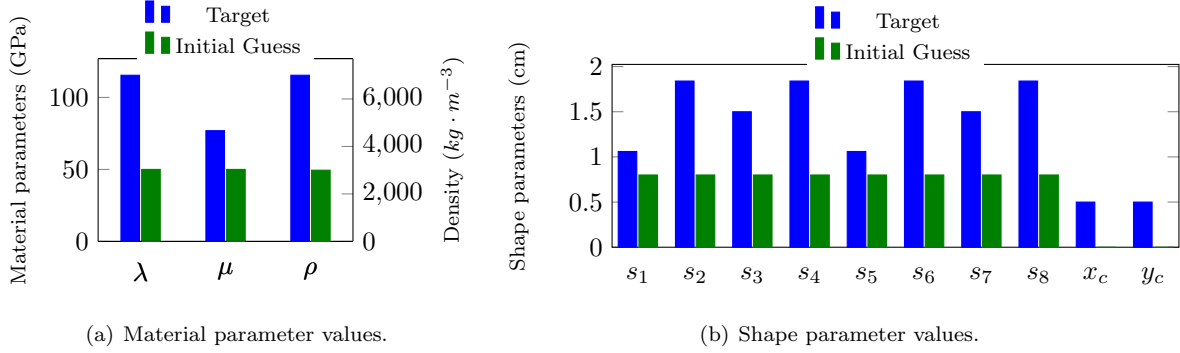(a) Material parameter values.   (b) Shape parameter values.

Figure 3: Characteristic parameter values for octogonal-shaped scatterer experiment. Target vs. Initial Guess.

Since the synthetic FFP measurements cannot be generated analytically, they were computed using the IPDG solver introduced in [64]. However, in order to avoid the inverse crime [1], we employed a mesh with a finer resolution than the one used during the inversion process.

To solve the considered thirteen-parameter inverse problem (see Eqs. (8), (10), and (11)), we used as an initial guess a regular convex octagon elastic scatterer $\Omega^{(0)}$ (see Fig. 2(b)) whose characteristic parameter values are reported in Fig.3. The results of this inversion experiment are also reported in Figs. 4-7. The following observations are noteworthy:

- The initial guess for the parameters values has been selected outside the pre-asymptotic convergence region, ensuring that the algorithm is *"blind"* to the sought-after thirteen values of the parameters, as reported in Table 3. Indeed, the initial relative errors in the shape parameters, Lamé coefficients, the density, and the origin of the scatterer, are about 53%, 51%, 62%, and 50%, respectively. These values lead to a computed initial FFP with a relative residual that exceeds 80% on the intensity and 115% on the FFP measurements.

- Fig. 4 illustrates the convergence performance of the algorithm. More specifically, the determination of the shape and material parameters (in Stage I) is completed after 18 iterations. The relative residual on the FFP intensity drops from above 80% to below 1%. In Stage II, i.e., the determination of the origin of the scatterer, the relative residual on the FFP drops from above 115% to below 1% after 13 iterations.

20
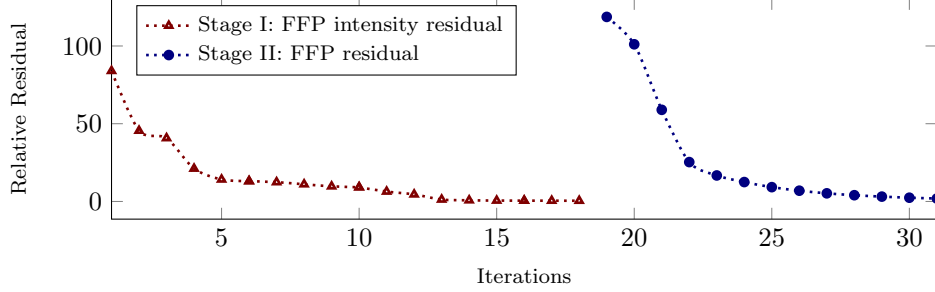
Figure 4: Convergence history in the case of the octogonal-shape scatterer experiment. $f = 55.7$kHz and noise free measurements.

- At convergence in Stage I, the algorithm delivers the shape parameters, the Lamé coefficients, and the density with relative errors of 0.08%, 2% and 0.5%, respectively (see Figs. 5(e)-6(e)). At convergence, i.e., at the end of Stage II, the location of the scatterer is retrieved with a relative error of about 2% (see Fig. 6(g)). Clearly, the proposed algorithm recovers all the parameter values with an impressive accuracy level.

- Stagnation phases occurred during the iterative process (see Figs. 5(a)-(e) and Figs. 6(a)-(e)). As stated earlier, lowering the regularized parameter values each time allows to reduce the FFP residuals to the tolerance level (below 1%).

- Note that the condition number of the linear system (11) without no regularization is about 10^{15}, whereas employing the proposed regularization procedure reduces it by 7 orders of magnitude.

5.1.2. Case of a mockup submarine

The goal here is to retrieve the characteristic parameter values of a mockup submarine made of *aluminum* (see 8(a)). The wet surface Γ of the considered elastic scatterer is represented by

$$\Gamma = \left\{ (x_c, y_c)^T + \sum_{k=1}^{M} r(\theta)(\cos\theta, \sin\theta)^T \quad ; \quad \theta \in [0, 2\pi) \right\}, \tag{17}$$

where r represents the polar radius whose expression is given by the following Fourier polynomial of order M:

$$r(\theta) = s_0 + \sum_{k=1}^{M} s_{2k-1} \cos k\theta + s_{2k} \sin k\theta \quad ; \quad \theta \in [0, 2\pi).$$

The values of the shape parameters s_j together with the center of the scatterer (x_c, y_c), as well as the material parameters (λ, μ, ρ) are reported in Fig. 9.
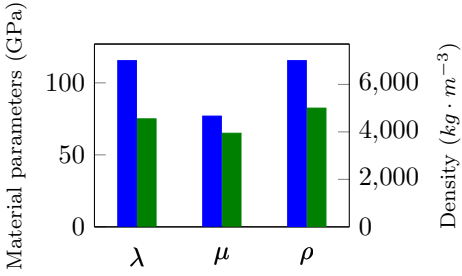
Similarly to the experiment pertaining to the non-convex octogonal scatterer, we have generated the synthetic FFP measurements points at frequency $f = 55.7$kHz using the IPDG solver introduced in [64]. Here again, in order to avoid the inverse crime [1], we employed a mesh finer than the one used during the inversion process.
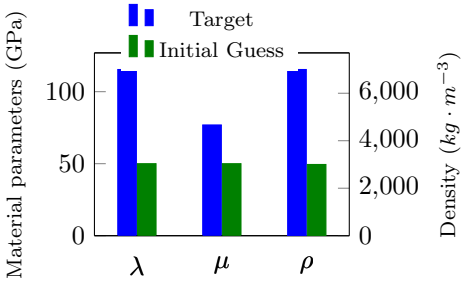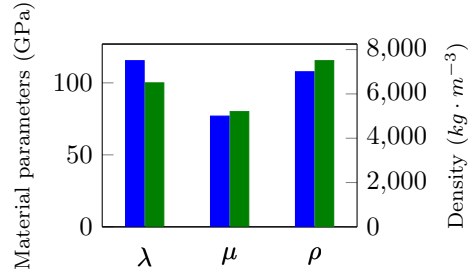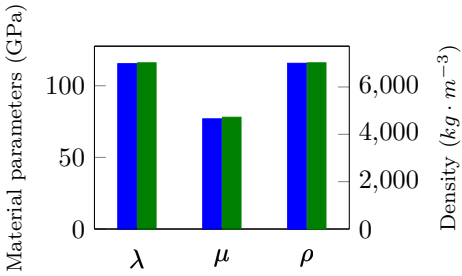
21

(a) Stage I: Iteration 0.
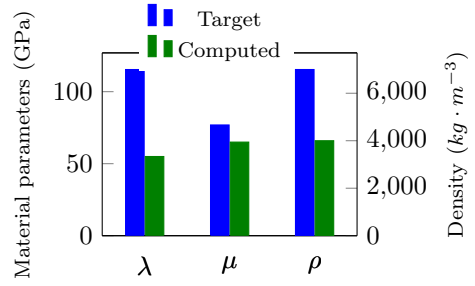
(b) Stage I: Iteration 6.

(c) Stage I: Iteration 10.

(d) Stage I: Iteration 16.

(e) Stage I: Iteration 18.

Figure 5: Material parameters for the octogonal-shaped scatterer experiment. Target vs. Computed Values at the occurred stagnation phases in Stage I. $f = 55.7\text{kHz}$ and noise free measurements.
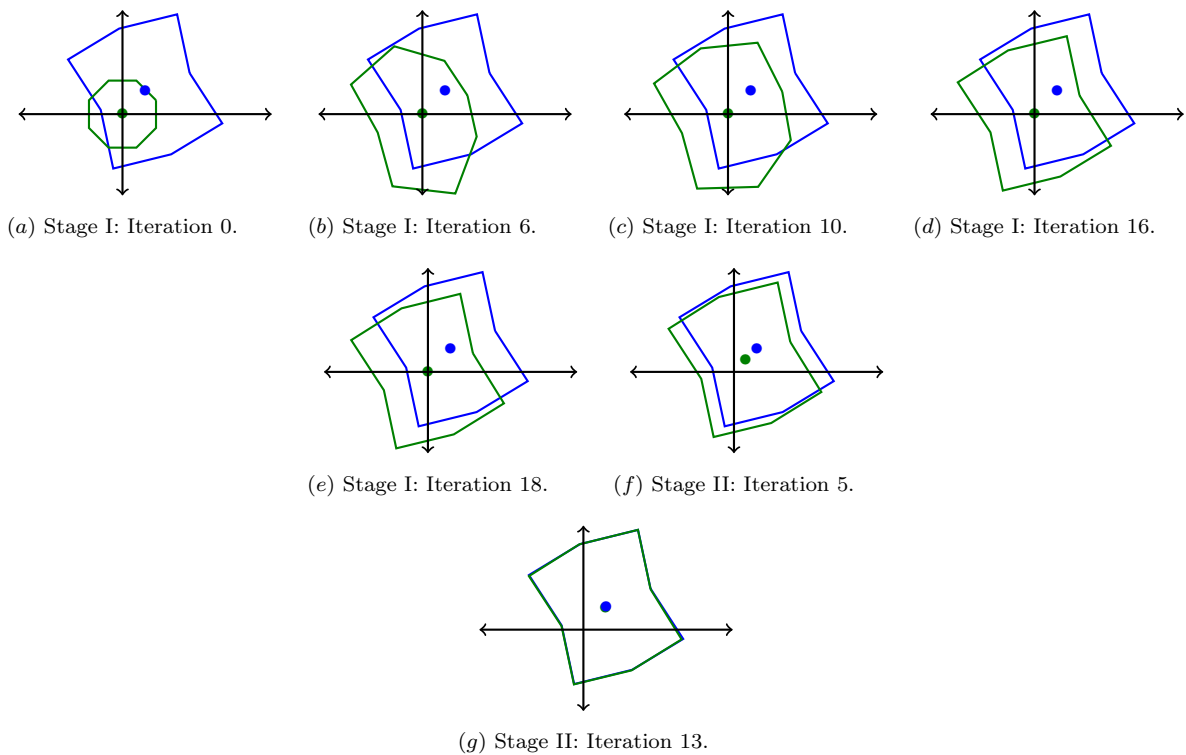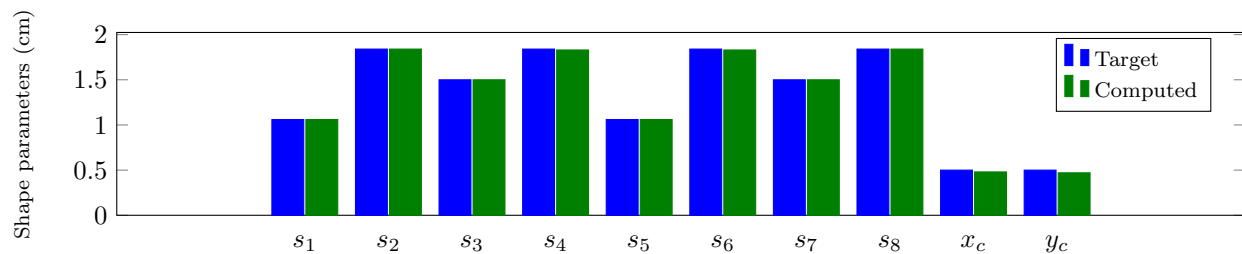
(a) Stage I: Iteration 0. (b) Stage I: Iteration 6. (c) Stage I: Iteration 10. (d) Stage I: Iteration 16.

(e) Stage I: Iteration 18. (f) Stage II: Iteration 5.

(g) Stage II: Iteration 13.

Figure 6: Shape and location of the octogonal-shaped scatterer experiment. Target vs. Computed Values at the occurred stagnations. $f = 55.7$kHz and noise free measurements.

Figure 7: Characteristic shape parameter values of the octogonal-shaped scatterer experiment. Target vs. Computed Values at convergence. $f = 55.7$kHz and noise free measurements.

(a) Target scatterer (b) Initial scatterer

Figure 8: Shape configurations for the mockup submarine experiments: Target vs. Initial Guess.

23

(a) Material parameter values. (b) Shape parameter values.
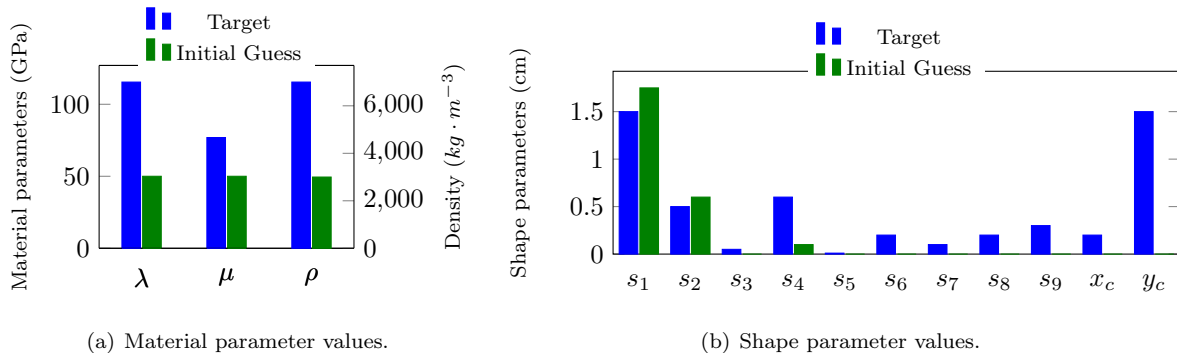
Figure 9: Characteristic parameter values for the mockup submarine scatterer experiment. Target vs. Initial Guess.

To solve the resulting 14-parameter inverse problem (see Eqs. (8), (10), and (11)), we applied the proposed multi-stage algorithm starting from an initial configuration $\Omega^{(0)}$ set to be a disk-shaped domain (see Fig. 8(b)). The characteristic parameter values of $\Omega^{(0)}$ are reported in Fig. 9 and the results of this numerical experiment are reported in Figs. 10-12. The following observations are noteworthy:

- The proposed algorithm is initiated outside the pre-asymptotic convergence region. Indeed, the considered initial configuration, a disk-shaped domain, differs significantly from the target configuration (see Figs. 9, 12(a)). The initial relative errors on the shape parameters, the origin parameters, Lamé coefficients, and the density are about 41%, 100%, 55%, and 85%, respectively. The initial relative residual on the FFP is of about 63% on the phaseless FFP measurements and of about 120% on the full FFP measurements.

- The convergence of the algorithm in this case is clearly demonstrated in Fig. 10. More specifically, Stage I is completed after 24 iterations. Indeed, the relative residual on the FFP intensity drops from 63% to 0.17%. Furthermore, the algorithm converges in Stage II after only 10 iterations. The relative residual on the full FFP measurements drops from 152% to 0.57%.

- Similarly to the previous numerical experiment, the algorithm recovers all the sought-after parameters of the mock-up submarine with an impressive accuracy level. Indeed, the relative errors on the computed shape parameters, Lamé coefficients, and the density are 0.43%, 1%, and 2.7%, respectively (see Fig. 11). The center (x_c, y_c) of submarine is recovered with a relative error of about 0.1% (see Fig. 12).

- The stagnation phenomenon also occurs here at several instances during the iteration process (see Figs. 11-12). This phenomenon is treated each time it happened by lowering the value of the regularization parameter.

- Similarly to the octagon experiment, the proposed multi-stage strategy algorithm is able to successfully recover all the parameters of the mockup submarine from the knowledge of the FFP measurements corresponding to only a single incident plane wave (i.e., one incident direction and one frequency). This success is most likely due to the fact that the employed data are measured over the full aperture.
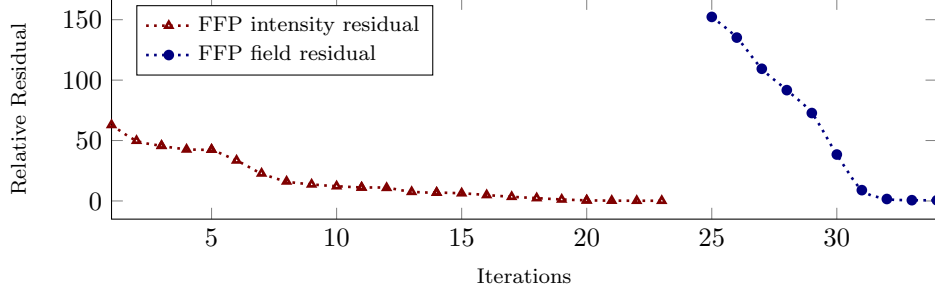
24

Figure 10: Convergence history for the mockup submarine scatterer experiment. $f = 55.7$kHz and noise free measurements.

- Note that the condition number of the linear system (11) without no regularization attains exploding values of orders 10^{28}, whereas employing the proposed regularization procedure reduces it to about 10^8.

### 5.2. Performance analysis in the presence of noise. Case of an octogonal-shaped scatterer

In what follows, we investigate the robustness and the accuracy of the proposed multi-stage solution methodology to the noise effect. We continue focusing on the parameter identification problems scenario. Due to space limitations, we present illustrative numerical results corresponding to only the octagon configuration given by Figs. 2 and 3. Results for other objects can be found in [71],

We analyze here the noise effect on the determination of the characteristic parameter values corresponding to the non convex elastic scatterer described in Fig. 2(a). To this end, we consider the same numerical experiment set up presented in section 5.1.1. The only difference here is that we add to the measured FFP white noise of three different levels: 5%, 10%, and 15%. The results reported in Table 1 clearly indicate that the proposed computational strategy exhibits high performance efficiency. Indeed, we observe that:

- For all three noise levels, the proposed computational methodology is initiated outside the pre-asymptotic convergence region. Indeed, the initial residuals on the phaseless FFP (resp. the full FFP) measurements, for all noise levels, exceed 80% (resp. 120%).

- For all noise levels, the sought-after parameters of the scatterer are retrieved with a high accuracy level, as reported in Table 1.

### 5.3. Recovery with multiple-frequency measurements. Case of a mockup submarine

We present here numerical results demonstrating, as it can be expected, that using FFP measurements corresponding to more than one frequency significantly improves the performance accuracy of the proposed algorithm. The improvement in the accuracy is remarkably noticeable when retrieving the material parameters with highly noisy data. Here also, we focus on the parameter identification problems scenario. We consider the thirteen parameters inverse problem introduced in section 5.1.2. Specifically, the goal is to recover the parameter's values of the mockup submarine made of aluminum depicted in Fig. 8(a). These
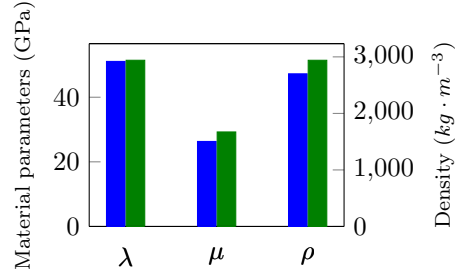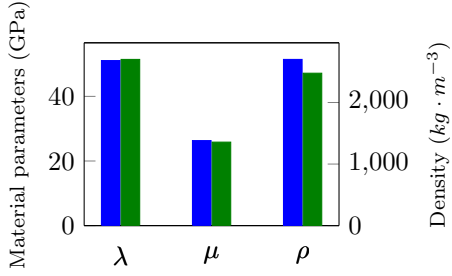
25
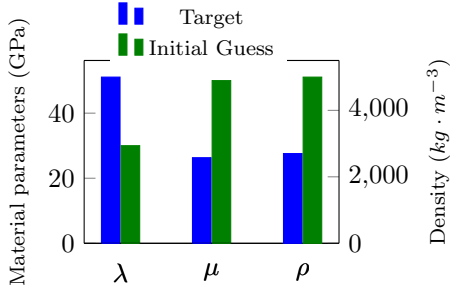
(a) Stage I: Iteration 0.
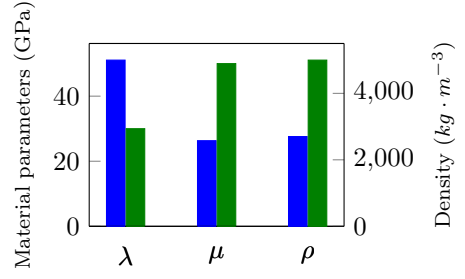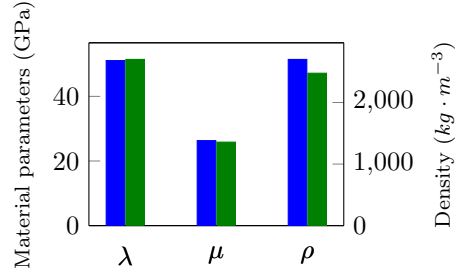

(b) Stage I: Iteration 3.
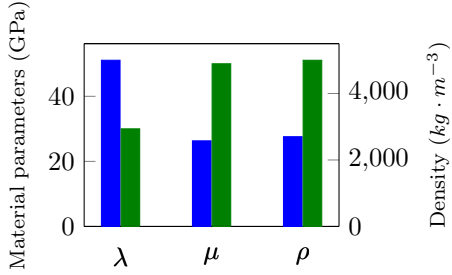
(c) Stage I: Iteration 11.

(d) Stage I: Iteration 14.

(e) Stage I: Iteration 20.

(f) Stage I: Iteration 23.

Figure 11: Material parameters for the mockup submarine scatterer experiment. Target vs. Computed Values at the occurred stagnation phases in Stage I. $f = 55.7\text{kHz}$ and noise free measurements.

Noise level	Relative Residual (%)		Relative Error (%)			
	Intensity	Field	Shape	Lamé	Density	Location
0%	1.02	1.88	1.02	2.61	0.47	1.53
5%	4.95	5.53	2.05	4.53	0.96	1.75
10%	10.98	12.77	4.64	9.14	11.58	3.87
15%	15.2	15.36	5.86	11.81	18.69	5.01

Table 1: Final relative residual and relative errors for the octogonal-shaped scatterer experiments for various noise levels and for frequency $f = 55.7\text{kHz}$.
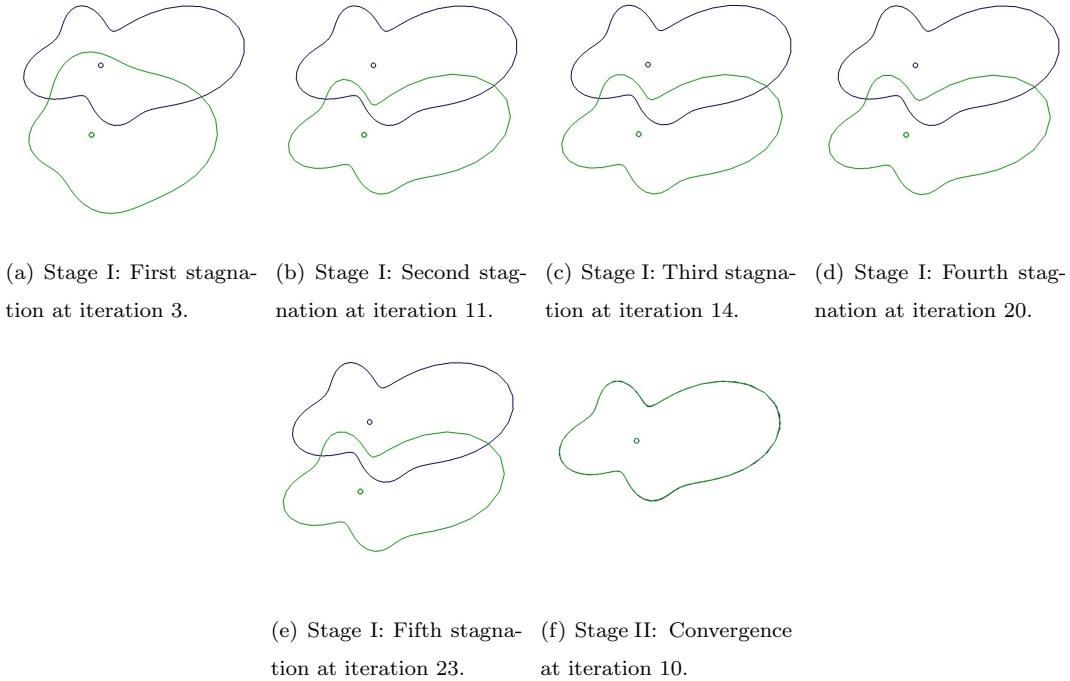
(a) Stage I: First stagna-   (b) Stage I: Second stag-   (c) Stage I: Third stagna-   (d) Stage I: Fourth stag-
tion at iteration 3.   nation at iteration 11.   tion at iteration 14.   nation at iteration 20.

(e) Stage I: Fifth stagna-   (f) Stage II: Convergence
tion at iteration 23.   at iteration 10.

Figure 12: Shape and location for the mockup submarine scatterer experiment. Target vs. Computed Values at the occurred stagnations. $f = 55.7$kHz and noise free measurements.

values are reported in Fig. 9. We initiate the algorithm from the same circular-shaped domain introduced in section 5.1.2 (see Fig. 8(b) and Fig. 9). We employed in this numerical experiments two sets of FFP measurements. We first apply the algorithm using FFP data corresponding to an angular frequency $\omega_1 = 0.35$, i.e., $f_1 = 55.7$kHz, the frequency regime used in section 5.1.2. When Stage II of the algorithm is completed, i.e., at convergence or stagnation, we re-apply the algorithm starting from the obtained final domain configuration, but this time using FFP measurements corresponding to a higher frequency regime $\omega_2 = 1$ ($f_2 = 159.15$kHz). Note that both sets of FFP measurements are tainted with white noise of level ranging from 0% to 15%. The results of these numerical experiments are reported in Table 2 and Fig. 13. These results suggest the following remarks:

- Similarly to all previous experiments, the algorithm is initiated outside the pre-asymptotic convergence region. Indeed, the initial configuration, a circular-shaped domain, differs significantly from the target mockup submarine, as indicated in Fig. 8.

- The accuracy on the shape parameters at convergence is quite satisfactory when employing the first frequency f_1, as reported in Table 2 and depicted in Fig. 13. On the other hand, the recovery of the material parameters and location is less accurate but still acceptable, as reported in Table 2. Given the quality of the reconstruction, one may even consider to stop the experiment at this step.

- Using FFP measurements for higher frequency ($f_2 = 159.15$kHz) and re-initiating the algorithm from

27

Frequency (kHz)	Noise level	Relative Residual (%)		Relative Error (%)			
		Intensity	Field	Shape	Lamé	Density	Location
	0%	0.17	0.57	0.43	4.96	1.15	0.12
$f_1 = 55.7$	**5**%	5.12	5.23	1.60	17.55	4.95	0.53
	10%	9.30	11.34	3.79	14.19	14.33	2.29
	15%	15.29	17.82	2.34	17.15	11.36	4.75
	0%	1.42	1.09	0.50	0.90	0.84	0.21
$f_2 = 159.15$	**5**%	4.05	6.46	0.53	0.89	0.90	0.21
	10%	12.76	13.05	3.75	2.52	0.68	1.66
	15%	13.01	14.62	2.33	6.74	8.37	0.91

Table 2: Relative Residual and Relative error for the mockup submarine scatterer for various noise levels in the measurements. Case of a reconstruction with two frequencies: $f_1 = 55.7$kHz and $f_2 = 159.15$kHz.

the computed configuration with the FFP data corresponding to the lower frequency ($f_1 = 55.7$kHz) enables to retrieve all the parameters with a quite remarkable accuracy, particularly for highly noisy measurements. Indeed, the accuracy on the material parameters is improved by a factor two to over an order of magnitude, depending on the noise level. Moreover, the accuracy level on the origin of the scatterer is significantly improved (the error is reduced by almost a factor 5 in the case of 15% noise level), as reported in Table 2 and Fig. 13.

5.4. Performance analysis in the case of an incomplete parametrization

We consider in this section the situation where the target obstacle cannot be described by the shape parametrization adopted for representing the trial solutions. Such problems are likely to be encountered in practical applications. To this end, we consider the octagon configuration given by Figs. 2(a)-3 and we employ the shape parametrization given by (16) but with only four shape parameters, that is, twice less shape parameters than for the identification parameter problem in Section 5.1. Hence, we attempt here to recover an obstacle that cannot be represented by the chosen parametrization. The selected shape parametrization contains only quadrilateral-shaped objects. This numerical experiment is of practical interest since for many realistic applications, one cannot expect to be able to describe the unknown scatterer with a parametrization chosen a priori. The obtained results depicted in Figs. 14-16 have been obtained with both noise free and 10% noisy measurements. The following remarks are noteworthy:

- The initial relative errors on the shape, the material parameters, and the location of the scatterer are about respectively 38%, 62%, and 50% respectively. Hence, the selected initial guess for the parameter values (See Fig. 15(a) and Fig. 16(a)) have been selected outside the pre-asymptotic convergence region.

(a) Noise level 0%.   (b) Noise level 5%.

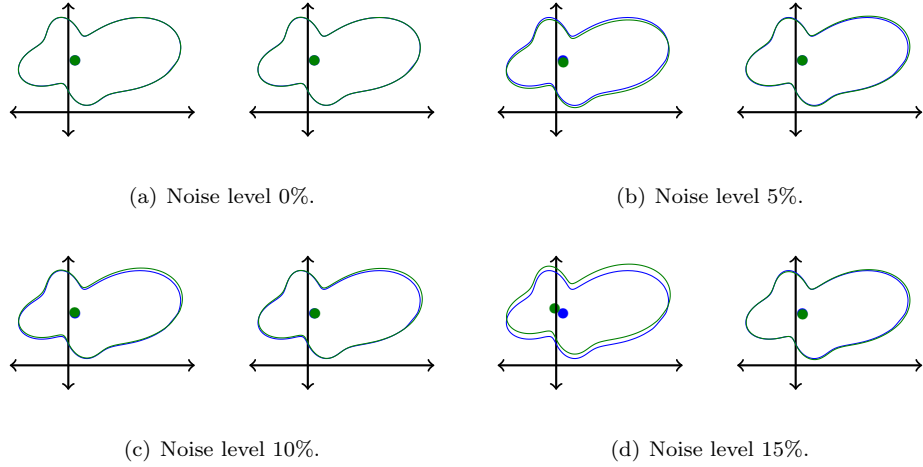(c) Noise level 10%.   (d) Noise level 15%.

Figure 13: Accuracy level on the shape and location parameters' values for the mockup submarine scatterer experiments. Sensitivity to the noise level in the measurements. Case of a two frequencies reconstruction: $f_1 = 55.7$kHz (right pictures) and $f_2 = 159.15$kHz (left pictures).

- Fig. 14 illustrates the convergence performance of the algorithm. More specifically, the determination of the shape and material parameters (in Stage I) is completed after 15 iterations with and without noise. The relative residual on the FFP intensity drops from above 87% to about 9% in the absence of the noise and to about 14% for 10% noisy measurements. In Stage II, i.e., the determination of the origin of the scatterer, the relative residual on the FFP drops, after 8 iterations from above 120% to about 28% in the absence of the noise and to about 29% for the noisy case.

- Fig. 15(b)-(c) and Fig. 16(b)-(c) show that at convergence in Stage I, the overall silhouette of the obstacle is well reproduced in spite of the fact that the trial shape parametrization contains only four vertices of the sought-after octagon. The algorithm is able to deliver the four shape parameters with a relatively good accuracy. Indeed, the relative error is about 8% without the noise and 7% in the noisy case. On the other hand, the accuracy level on the Lamé coefficients, and the density is respectively 31% and 28% without the noise and 28% and 33% with the noise. This is not surprising since the accuracy of the material parameters is very sensitive to the one the shape of the corresponding elastic object. Moreover, the location of the scatterer is retrieved in Stage II with a relative error of about 17% for both cases (see Fig. 15(b)-(c)).

5.5. Performance analysis in the case of blind problems

We consider in this section the situation where little a priori information on the shape of the target object is available. This problem falls into the category of blind problems where a more generic parametrization is needed to capture a wider class of shapes. We focus in this section on the octagonal-shaped object introduced in Section 5.1 and investigate the performance of the proposed method in the case of two parametrizations:
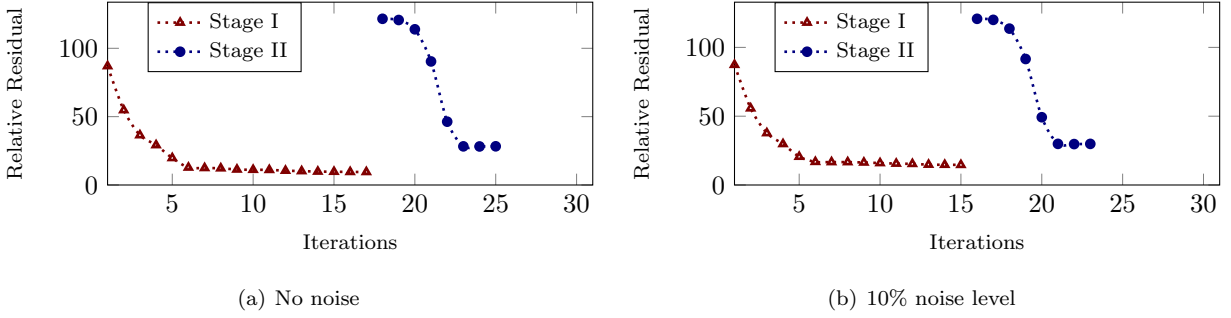
29

(a) No noise   (b) 10% noise level

Figure 14: Convergence history for the octogonal-shape scatterer experiment with an incomplete parametrization (four shape parameters) and FFP measurements corresponding to $f = 55.7 kHz$.

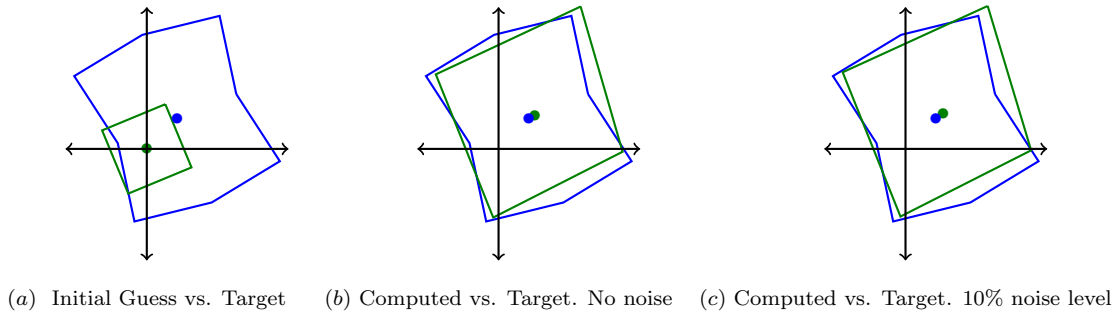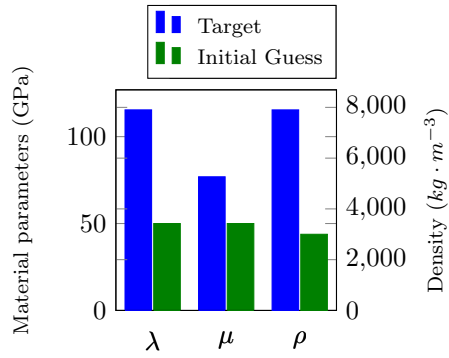(a) Initial Guess vs. Target   (b) Computed vs. Target. No noise   (c) Computed vs. Target. 10% noise level
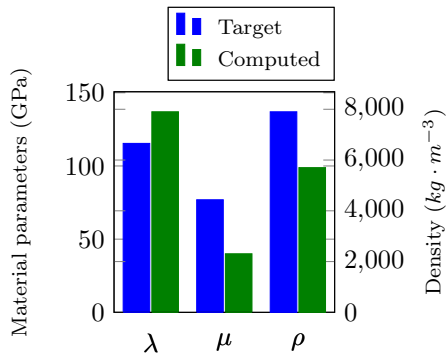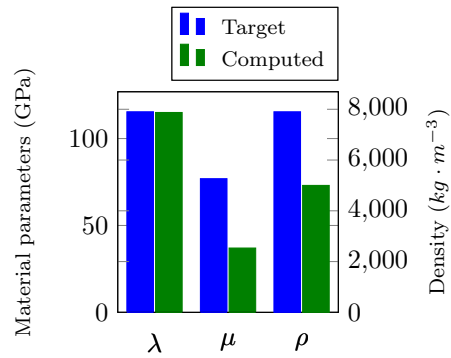
Figure 15: Accuracy level on the shape and location parameters' values for octogonal-shaped scatterer experiments with incomplete parametrization (four shape parameters). $f = 55.7 kHz$.

(a) Initial Guess vs. Target

(b) Computed vs. Target. No Noise

(c) Computed vs. Target. Noise level 10%

Figure 16: Material parameters for the octogonal-shaped scatterer experiment with an incomplete parametrization (four pshape parameters). $f = 55.7$kHz.

the piecewise linear parametrization and the Fourier-type parametrization

5.5.1. Reconstruction with the piecewise-linear parametrization

We focus on the reconstruction of the shape of the octagon introduced in Section 5.1 and employ the shape parametrization given by (16) for representing the trial solutions but this time with 16 parameters, thai is twice more shape parameters than needed. Hence, the only information available is that the sought-after object is a polygon with at most 16 sides, as illustrated by the choice of the initial guess. We report on the reconstruction of the octagon in the case where the FFP measurements are (a) noise free and (b) tainted with a 10% white noise level. The obtained results are depicted in Figs. 17-19. We observe the following:

- The initial relative error on the shape is about 53% and the corresponding initial relative residual is about 82% (resp. 86%) for noise free (resp. 10% noisy) measurements. This clearly shows that the proposed algorithm is starting outside the pre-asymptotic convergence region.

- The reconstruction of the shape requires using successively three frequencies in the absence of the noise and two with noisy measurements, as indicated in Figs. 17-19.

- In both cases the algorithm converges. The initial relative residual drops to about .16% (resp. 15%) in the absence (resp. the presence) of the noise.

- The shape of the octagon is retrieved with a very high accuracy level in both cases. Indeed, the relative error at convergence is about .2% (resp. 6.6%) in the absence (resp. the presence) of the noise.
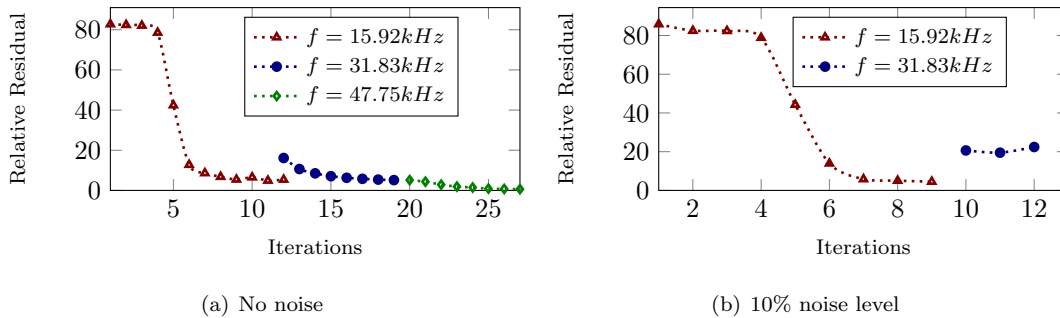

(a) No noise

(b) 10% noise level

Figure 17: Convergence history for the octogonal-shape scatterer experiment with 16 parameters and and FFP measurements corresponding to multiple frequencies. Sensitivity to the noise.

5.5.2. Reconstruction with Fourier-type parametrization

We continue focusing on the reconstruction of the shape of the octagon introduced in Section 5.1 but this time we employ the Fourier parametrization given by (17) for representing the trial solutions. This is a situation where we do not know if the target is a polygon or a disk. We report on the reconstruction of the octagon in the case where the FFP measurements are (a) noise free and (b) tainted with a 10% white noise level. The obtained results are depicted in Figs. 20-22. We observe the following:
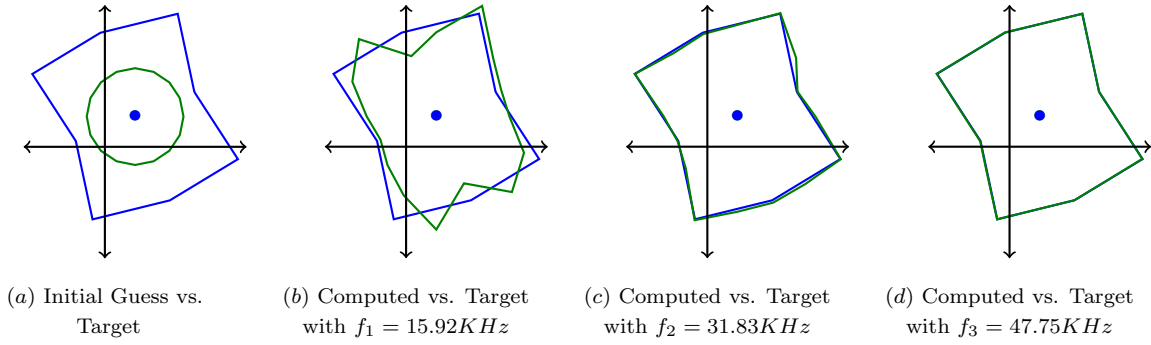
(a) Initial Guess vs. Target

(b) Computed vs. Target with $f_1 = 15.92KHz$

(c) Computed vs. Target with $f_2 = 31.83KHz$

(d) Computed vs. Target with $f_3 = 47.75KHz$

Figure 18: Accuracy level on the shape for the octogonal-shape scatterer experiment with 16 parameters. Case of a three-frequency successive reconstruction with noise free measurements.

(a) Initial Guess vs. Target

(b) Computed vs. Target with $f_1 = 15.92KHz$

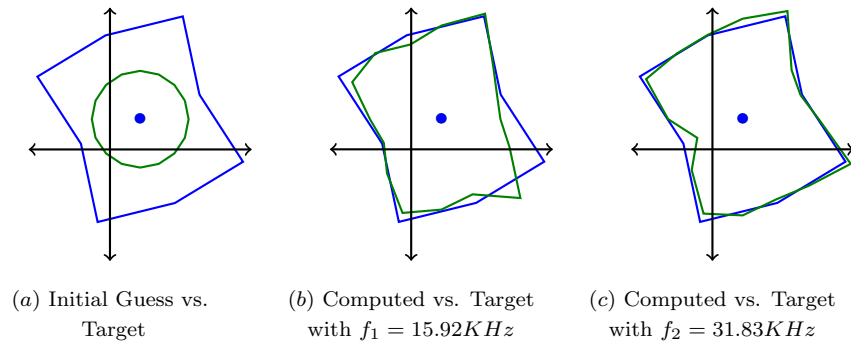(c) Computed vs. Target with $f_2 = 31.83KHz$

Figure 19: Accuracy level on the shape for the octogonal-shape scatterer experiment with 16 parameters. Case of a two-frequency successive reconstruction with measurements tainted with 10% of white noise.

- The initial guess is a disk and the corresponding initial relative residual is about 82% (resp. 83%) for noise free (resp. 10% noisy) measurements. This clearly shows that the proposed algorithm is starting outside the pre-asymptotic convergence region.

- The reconstruction of the shape requires using successively two frequencies in the absence of the noise and only one with noisy measurements, as indicated in Figs. 20-22.

- In both cases the algorithm converges. The initial relative residual drops to about 0.9% (resp. 11%) in the absence (resp. the presence) of the noise.

- The silhouette of the octagon is very well reproduced in both cases. Indeed, the relative error at convergence is about 6.9% (resp. 7.2%) in the absence (resp. the presence) of the noise.
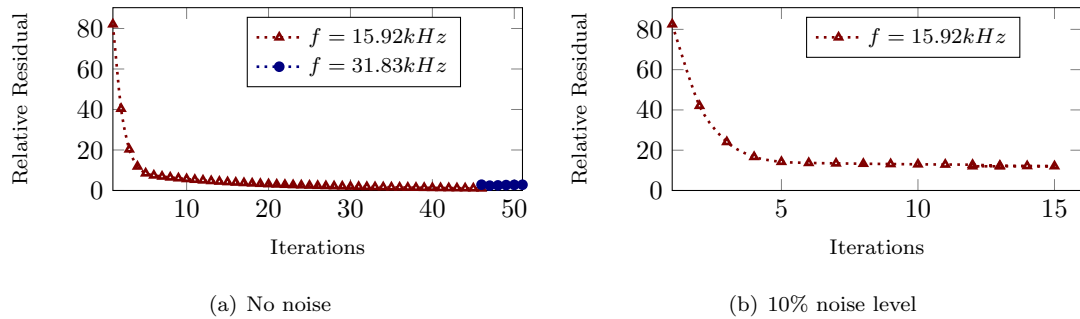

(a) No noise

(b) 10% noise level

Figure 20: Convergence history for the octogonal-shape scatterer experiment with Fourier parametrization and FFP measurements corresponding to multiple frequencies. Sensitivity to the noise.

(a) Initial Guess vs. Target

(b) Computed vs. Target with $f_1 = 15.92 KHz$

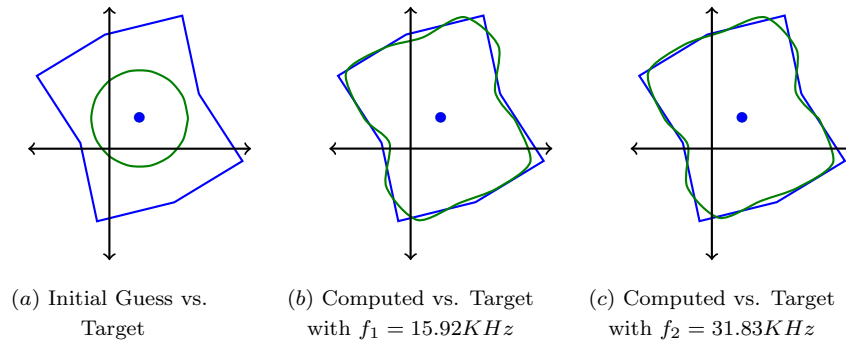(c) Computed vs. Target with $f_2 = 31.83 KHz$

Figure 21: Accuracy level on the shape for the octogonal-shape scatterer experiment with Fourier parametrization. Case of a two-frequency successive reconstruction with noise free measurements.

6. Conclusions & Remarks

We have designed a solution methodology for retrieving all the parameters characterizing an elastic scatterer from its corresponding FFP measurements. To the best of our knowledge, this is the first attempt
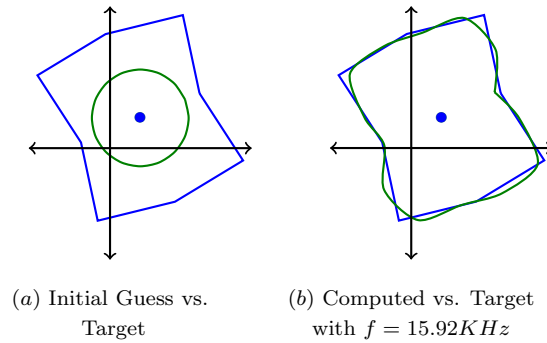
34

(*a*) Initial Guess vs. Target

(*b*) Computed vs. Target with $f = 15.92 KHz$

Figure 22: Accuracy level on the shape for the octogonal-shape scatterer experiment with Fourier parametrization. Case of a mono-frequency reconstruction with FFP measurements tainted with 10% of white noise.

to solve numerically this challenging time-harmonic inverse scattering problem, a relevant problem to various real-world applications. The proposed numerical approach is a multi-stage iterative procedure in which a carefully designed regularized Newton-type algorithm plays a central role. The reported numerical results clearly demonstrated the effectiveness of the proposed computational strategy for solving this important class of inverse problems, even when the data are highly noisy.

7. Bibliography

References

[1] D. Colton, R. Kress, Inverse acoustic and electromagnetic scattering theory, Vol. 93, Springer Science & Business Media, 2012.

[2] J. Hadamard, Lectures on Cauchy's problem in linear partial differential equations, Courier Corporation, 2014.

[3] A. Fichtner, Full seismic waveform modelling and inversion, Springer Science & Business Media, 2010.

[4] A. Tarantola, Inverse problem theory and methods for model parameter estimation, Vol. 89, Siam, 2005.

[5] F. Le Chevalier, Principles of radar and sonar signal processing, Artech House, 2002.

[6] A. Walther, The ray and wave theory of lenses, Vol. 15, Cambridge University Press, 1995.

[7] T. Levin, E. Turkel, D. Givoli, Obstacle identification using the TRAC algorithm with a second-order ABC, International Journal for Numerical Methods in Engineering 118 (2) (2019) 61–92.

[8] D. Colton, J. Coyle, P. Monk, Recent developments in inverse acoustic scattering theory, Siam Review 42 (3) (2000) 369–414.

[9] C. Farhat, R. Tezaur, R. Djellouli, On the solution of three-dimensional inverse obstacle acoustic scattering problems by a regularized Newton method, Inverse problems 18 (5) (2002) 1229.

35

[10] F. Cakoni, D. Colton, Qualitative methods in inverse scattering theory: An introduction, Springer Science & Business Media, 2005.

[11] O. Ivanyshyn, Shape reconstruction of acoustic obstacles from the modulus of the far field pattern, Inverse Problems and Imaging 1 (4) (2007) 609.

[12] R. Djellouli, Inverse acoustic problems, in: F. Magoulès (Ed.), Computational methods for acoustics problems, Saxe-Coburg Publications, Stirlingshire (UK), 2008, pp. 263–294.

[13] J. Elschner, G. C. Hsiao, A. Rathsfeld, An optimization method in inverse acoustic scattering by an elastic obstacle, SIAM Journal on Applied Mathematics 70 (1) (2009) 168–187.

[14] P. Monk, V. Selgas, Near field sampling type methods for the inverse fluid–solid interaction problem, Inverse Problems & Imaging 5 (2) (2011) 465–483.

[15] F. Cakoni, D. Colton, P. Monk, Qualitative methods in inverse electromagnetic scattering theory: Inverse scattering for anisotropic media., IEEE Antennas and Propagation Magazine 59 (5) (2017) 24–33.

[16] M. V. Klibanov, V. G. Romanov, Reconstruction procedures for two inverse scattering problems without the phase information, SIAM Journal on Applied Mathematics 76 (1) (2016) 178–196.

[17] H. Qin, X. Liu, The linear sampling method for inhomogeneous medium and buried objects from far field measurements, Applied Numerical Mathematics 105 (2016) 82–95.

[18] H. Barucq, F. Faucher, H. Pham, Localization of small obstacles from back-scattered data at limited incident angles with full-waveform inversion, Journal of Computational Physics 370 (2018) 1–24.

[19] Y. Olshansky, E. Turkel, Simultaneous scatterer shape estimation and partial aperture far-field pattern denoising, Communications in Computational Physics 11 (2) (2012) 271–284.

[20] A. B. Bakushinsky, M. Y. Kokurin, Iterative methods for approximate solution of inverse problems, Vol. 577, Springer Science & Business Media, 2005.

[21] R. Kress, W. Rundell, A quasi-Newton method in inverse obstacle scattering, Inverse Problems 10 (5) (1994) 1145.

[22] L. Mönch, A Newton method for solving the inverse scattering problem for a sound-hard obstacle, Inverse Problems 12 (3) (1996) 309.

[23] C. Pöppe, R. D. Murch, D. G. H. Tan, D. J. N. Wall, M. V. Klibanov, J. Malinsky, Newton-Kantorovich method applied to two-dimensional inverse scattering for an exterior Helmholtz problem, Inverse Problems 5 (1989) 1173.

[24] W. Tobocman, Inverse acoustic wave scattering in two dimensions from impenetrable targets, Inverse Problems 5 (6) (1989) 1131.

[25] S. L. Wang, Y. M. Chen, An efficient numerical method for exterior and interior inverse problems of Helmholtz equation, Wave Motion 13 (4) (1991) 387–399.

[26] R. Kress, Integral equation methods in inverse obstacle scattering, Engineering analysis with boundary elements 15 (2) (1995) 171–179.

[27] T. S. Angell, D. Colton, A. Kirsch, The three dimensional inverse scattering problem for acoustic waves, Journal of Differential Equations 46 (1) (1982) 46–58.

[28] G. Kristensson, Inverse problems for acoustic waves using the penalised likelihood method, Inverse Problems 2 (4) (1986) 461.

[29] M. V. Klibanov, A. E. Kolesov, Convexification of a 3-d coefficient inverse scattering problem, Computers & Mathematics with Applications 77 (6) (2019) 1681–1702.

[30] M. V. Klibanov, A. E. Kolesov, D.-L. Nguyen, Convexification method for an inverse scattering problem and its performance for experimental backscatter data for buried targets, SIAM Journal on Imaging Sciences 12 (1) (2019) 576–603.

[31] G. Beylkin, R. Burridge, Linearized inverse scattering problems in acoustics and elasticity, Wave motion 12 (1) (1990) 15–52.

[32] J. E. Warner, M. I. Diaz, W. Aquino, M. Bonnet, Inverse material identification in coupled acoustic-structure interaction using a modified error in constitutive equation functional, Computational mechanics 54 (3) (2014) 645–659.

[33] S. Hubmer, E. Sherina, A. Neubauer, O. Scherzer, Lamé parameter estimation from static displacement field measurements in the framework of nonlinear inverse problems, SIAM Journal on Imaging Sciences 11 (2) (2018) 1268–1293.

[34] A. Lechleiter, J. W. Schlasche, Identifying Lamé parameters from time-dependent elastic wave measurements, Inverse Problems in Science and Engineering 25 (1) (2017) 2–26.

[35] H. Ammari, E. Iakovleva, D. Lesselier, A MUSIC algorithm for locating small inclusions buried in a half-space from the scattering amplitude at a fixed frequency, Multiscale Modeling & Simulation 3 (3) (2005) 597–628.

[36] O. Ivanyshyn, R. Kress, Identification of sound-soft 3D obstacles from phaseless data, Inverse Problems and Imaging 4 (1) (2010) 131–149.

[37] R. Fazli, M. Nakhkash, An analytical approach to estimate the number of small scatterers in 2D inverse scattering problems, Inverse Problems 28 (7) (2012) 075012.

[38] Y. Zhang, A. A. Oberai, P. E. Barbone, I. Harari, Solution of the time-harmonic viscoelastic inverse problem with interior data in two dimensions, International journal for numerical methods in engineering 92 (13) (2012) 1100–1116.

[39] R. Griesmaier, C. Schmiedecke, A multifrequency MUSIC algorithm for locating small inhomogeneities in inverse scattering, Inverse Problems 33 (3) (2017) 035015.

[40] B. Zhang, H. Zhang, Recovering scattering obstacles by multi-frequency phaseless far-field data, Journal of Computational Physics 345 (2017) 58–73.

[41] D. Zhang, Y. Guo, Uniqueness results on phaseless inverse acoustic scattering with a reference ball, Inverse Problems 34 (8) (2018) 085002.

[42] L. Bourgeois, N. Chaulet, H. Haddar, On simultaneous identification of the shape and generalized impedance boundary condition in obstacle scattering, SIAM Journal on Scientific Computing 34 (3) (2012) A1824–A1848.

[43] E. Amitt, D. Givoli, E. Turkel, Combined arrival-time imaging and time reversal for scatterer identification, Computer Methods in Applied Mechanics and Engineering 313 (2017) 279–302.

[44] M. C. Junger, D. Feit, Sound, structures, and their interaction, Vol. 225, MIT press Cambridge, MA, 1986.

[45] H. Barucq, R. Djellouli, E. Estecahandy, On the existence and the uniqueness of the solution of a fluid–structure interaction scattering problem, Journal of Mathematical Analysis and applications 412 (2) (2014) 571–588.

[46] T. Hargé, Valeurs propres d'un corps élastique, Comptes rendus de l'Académie des sciences. Série 1, Mathématique 311 (13) (1990) 857–859.

[47] I. Azpiroz, H. Barucq, R. Djellouli, H. Pham, Characterization of partial derivatives with respect to material parameters in a fluid-solid interaction problem, Journal of Mathematical Analysis and Applications 465 (2) (2018) 903–927.

[48] H. Barucq, R. Djellouli, E. Estecahandy, M. Moussaoui, Mathematical determination of the Fréchet derivative with respect to the domain for a fluid-structure scattering problem: Case of polygonal-shaped domains, SIAM Journal on Mathematical Analysis 50 (1) (2018) 1010–1036.

[49] C. J. Luke, P. A. Martin, Fluid–solid interaction: acoustic scattering by a smooth elastic obstacle, SIAM Journal on Applied Mathematics 55 (4) (1995) 904–922.

[50] I. Azpiroz, Contribution to the numerical reconstruction in inverse elasto-acoustic scattering, Ph.D. thesis, Université de Pau et des Pays de l'Adour (2018).

[51] D. Colton, A. Kirsch, A simple method for solving inverse scattering problems in the resonance region, Inverse problems 12 (4) (1996) 383.

[52] R. Kress, W. Rundell, Inverse obstacle scattering with modulus of the far field pattern as data, Inverse problems in medical imaging and nondestructive testing (1997) 75–92.

[53] O. Ivanyshyn, R. Kress, Inverse scattering for surface impedance from phase-less far field data, Journal of Computational Physics 230 (9) (2011) 3443–3452.

[54] H. W. Engl, M. Hanke, A. Neubauer, Regularization of inverse problems, Vol. 375, Springer Science & Business Media, 1996.

[55] S. F. Gilyazov, N. Gol'dman, Regularization of ill-posed problems by iteration methods, Vol. 499, Springer Science & Business Media, 2013.

[56] A. N. Tikhonov, V. Y. Arsenin, Methods for solving ill-posed problems, John Wiley and Sons, Inc, 1977.

[57] A. N. Tikhonov, Regularization of incorrectly posed problems, in: Soviet Mathematics Doklady, Vol. 4, 1963, pp. 1624–1627.

[58] H. Barucq, R. Djellouli, E. Estecahandy, Fréchet differentiability of the elasto-acoustic scattered field with respect to Lipschitz domains, Mathematical Methods in the Applied Sciences 40 (2) (2017) 404–414.

[59] P. G. Ciarlet, The finite element method for elliptic problems, Vol. 40, SIAM, 2002.

[60] X. Antoine, H. Barucq, A. Bendali, Bayliss–turkel-like radiation conditions on surfaces of arbitrary shape, Journal of Mathematical Analysis and Applications 229 (1) (1999) 184–211.

[61] A. Bayliss, E. Turkel, Radiation boundary conditions for wave-like equations, Communications on Pure and applied Mathematics 33 (6) (1980) 707–725.

[62] Z. Chen, X. Wu, An adaptive uniaxial perfectly matched layer method for time-harmonic scattering problems, Numer. Math. Theor. Meth. Appl 1 (2008) 113–137.

[63] H. Barucq, J. Diaz, V. Duprat, Long-term stable acoustic absorbing boundary conditions for regular-shaped surfaces, Tech. rep., RR-8203,INRIA hal-00776058 (2013).

[64] H. Barucq, R. Djellouli, E. Estecahandy, Efficient DG-like formulation equipped with curved boundary edges for solving elasto-acoustic scattering problems, International Journal for Numerical Methods in Engineering 98 (10) (2014) 747–780.

[65] P. R. Amestoy, I. S. Duff, J.-Y. L'Excellent, J. Koster, A fully asynchronous multifrontal solver using distributed dynamic scheduling, SIAM Journal on Matrix Analysis and Applications 23 (1) (2001) 15–41.

[66] P. R. Amestoy, A. Guermouche, J.-Y. L'Excellent, S. Pralet, Hybrid scheduling for the parallel solution of linear systems, Parallel computing 32 (2) (2006) 136–156.

[67] V. A. Morozov, On the solution of functional equations by the method of regularization, in: Doklady Akademii Nauk, Vol. 167, Russian Academy of Sciences, 1966, pp. 510–512.

[68] V. A. Morozov, Choice of parameter for the solution of functional equations by the regularization method, in: Sov. Math. Doklady, Vol. 8, Russian Academy of Sciences, 1967, pp. 1000–1003.

[69] G. Wahba, Spline models for observational data, Vol. 59, Siam, 1990.

[70] P. C. Hansen, D. P. O'Leary, The use of the L-curve in the regularization of discrete ill-posed problems, SIAM Journal on Scientific Computing 14 (6) (1993) 1487–1503.

[71] I. Azpiroz, H. Barucq, J. Diaz, R. Djellouli, Full determination of elastic scatterer characteristics from FFP measurements, Research Report RR-9247, Inria (2019).
URL https://hal.inria.fr/hal-01976990